Journal of
Materials Chemistry A

Materials for energy and sustainability

Accepted Manuscript

This article can be cited before page numbers have been issued, to do this please use: W. Yu, W. Shang, P. Tan, B. Chen, Z. Wu, H. Xu, Z. Shao, M. Liu and M. Ni, *J. Mater. Chem. A*, 2019, DOI: 10.1039/C9TA10658H.

ROYAL SOCIETY OF CHEMISTRY

rsc.li/materials-a

Toward a New Generation of Low Cost, Efficient, and Durable Metal-Air Flow Batteries

Wentao Yu[a], Wenxu Shang[a], Peng Tan[a*], Bin Chen[b], Zhen Wu[c,d], Haoran Xu[d], Zongping Shao[e,f], Meilin Liu[g], Meng Ni[d,h*]

a. Department of Thermal Science and Energy Engineering, University of Science and Technology of China, Hefei 230026, Anhui, China.
b. Institute of Deep Earth Sciences and Green Energy, Shenzhen University, Shenzhen, 518060, China.
c. Shaanxi Key Laboratory of Energy Chemical Process Intensification, School of Chemical Engineering and Technology, Xi'an Jiaotong University, Xi'an, 710049, Shaanxi, China.
d. Department of Building and Real Estate, The Hong Kong Polytechnic University, Hung Hom, Kowloon, Hong Kong, China.
e. Jiangsu National Synergetic Innovation Center for Advanced Material, College of Energy, State Key Laboratory of Materials-Oriented Chemical Engineering, Nanjing Tech University, Nanjing 210009, China.
f. Department of Chemical Engineering, Curtin University, Perth, WA 6845, Australia.
g. School of Materials Science and Engineering, Center for Innovative Fuel Cell and Battery Technologies, Georgia Institute of Technology, Atlanta, GA 30332-0245, USA.
h. Environmental Energy Research Group, Research Institute for Sustainable Urban Development (RISUD), The Hong Kong Polytechnic University, Hung Hom, Kowloon, Hong Kong, China.

* Corresponding authors:
Email: pengtan@ustc.edu.cn (Peng Tan)
Email: meng.ni@polyu.edu.hk (Meng Ni)

Abstract

Over the past decades, metal-air flow batteries (MAFBs) have attracted great attention as a promising candidate for the next-generation energy storage systems because of their potential to offer both high performance and scale flexibility, derived from the high energy density of metal-air batteries and the scalability of redox flow batteries. In this article, recent progress of metal-air flow batteries is overviewed, focusing on the structural designs and the advances in materials development. To get an insightful

View Article Online
DOI: 10.1039/C9TA10658H

view of the battery features, different categories are introduced on the basis of flow media, working principles, and configurations. In addition, detailed discussion about metal-air flow batteries with aqueous and non-aqueous electrolytes are conducted, containing advances in the structural design and material developments of metal electrodes, air electrodes, and electrolytes. Finally, the challenges and perspectives for future developments are synoptically presented.

1. Introduction

In recent years, climate change and the ever-increasing demands for energy have promoted the development of renewable energy sources (e.g., wind, solar, and water power).[1] Owing to the intermittent nature of these energy sources, large-scale and high-performance energy storage systems are in great need. Among various alternative technologies such as supercapacitors,[2–7] compressed air,[8–11] phase change,[12–14] and pumped hydro energy storage devices,[15–17] batteries are still one of the most promising energy storage devices due to the flexibility and stability.[18] Lithium-ion batteries (LIBs) have been widely used in many applications, notably for portable electronics and electric vehicles due to the remarkable energy densities.[19–21] LIBs have also been used for stationary applications, but the high cost and heat problems of LIBs make it urgent to develop new energy storage systems for large-scale power grids.[20,22–25] Metal-air batteries (MABs), which use oxygen from the ambient air as one reactant and pure metal as the other reactant, offer very high energy density. Since oxygen can be taken from air, the theoretical capacity of a MAB is determined largely by the amount of metal used. Thus, the theoretical capacity of a

View Article Online
DOI: 10.1039/C9TA10658H

zinc-air battery (ZAB) is ~820 mAh g−1 Zn, which is several times higher than those of widely used LIBs.[26] For a lithium-air battery (LAB), the theoretical capacity is ~3,860 mAh g−1 Li.[27] Regardless of the attractive prospects of MABs, however, many intrinsic problems still remain for practical applications. Similar to other secondary batteries using pure metals, dendrite formation is a critical challenge, which dramatically degrades the safety and stability. Passivation of metal electrodes due to adhesion of insoluble products and by-products is another critical challenge, resulting in degradation in battery performance. For the porous air electrodes, the performance is often limited by the availability of surface sites for electrode reactions and the resistance to transport of ions, electrons, and gases to or away from the reaction sites during charge and discharge. More importantly, the formation of insoluble products and by-products, especially in non-aqueous MABs (e.g., LABs), may block the path for gas transport and/or cover the active sites for electrode reactions, degrading battery performance during operation. In addition, the oxygen reduction reaction (ORR) during discharge and the oxygen evolution reaction (OER) during charge are multi-step, multi-electron transfer processes, and their sluggish kinetics drag the energy output and deteriorate the energy efficiency and coulombic efficiency.[28] Notwithstanding these challenges, significant progress has been achieved in three areas: i) developing high-performance battery materials (e.g., catalysts and stable electrolytes);[29–34] ii) designing new nanostructures or optimizing cell designs (e.g., nano-structured catalysts, fluidic electrode designs);[35–40] iii) combining MABs with other batteries to form hybrid systems, such as hybrid Zn-M/air batteries (M

View Article Online
DOI: 10.1039/C9TA10658H

represents transition metals),[41–48] and photo-assisted batteries.[49,50] In spite of these efforts, the commercialization of MABs still has a long way to go.

Redox flow batteries (RFBs) use external tanks to store electrolytes and reaction redox couples. Thus, the energy of the redox couples dissolved in the electrolytes is stored in separate storage tanks, not in the electrode materials of the RFB, which act only as the active reaction zones and current collectors, effectively eliminating many problems of the air electrodes discussed earlier. Also, the power and the energy are no longer coupled because the electrolyte and electroactive materials are stored separately.[51] These features greatly improve the convenience for enlarging the scale of the battery, making RFBs attractive for large-scale applications [52–54] Since the first Fe-Cr redox flow battery (Fe^{2+}/Fe^{3+}, Cr^{2+}/Cr^{3+}) proposed in the 1970s,[55] various types of RFBs have been developed, such as Sn-Fe,[56] Fe-Cr,[57,58] and vanadium-based RFBs,[58–62] Although significant progress from materials to structure designs has been made in VRFBs,[63–65] many problems still remain to be addressed, including narrow operational temperature window (10 to 40 ^{o}C), low energy density (< 25 Wh L–1 electrolyte), and limited stability and solubility of redox couples.[51,66–68]

Due to the forced convection of the electrolyte enabled by the circulation sub-system, the mass transfer is dramatically enhanced in RFBs. Therefore, when applying the flow system to MABs, many aforementioned problems in MABs and conventional RFBs can be well solved. First, a relatively high energy density is obtainable for a metal-air flow battery (MAFB) due to the relatively high energy density of a MAB than a conventional RFB. Second, MAFBs are more compact than

View Article Online
DOI: 10.1039/C9TA10658H

conventional RFBs. For conventional RFBs such as VRFBs, two redox couples, employed for electrode reactions, are stored in two separate storage tanks to avoid cross-contaminations. Conversely, the reactants of MAFBs are metals and ambient air, which means that the circulating electrolytes are just for enhancing mass transfer and bringing out products and by-products. Hence, only one storage tank is needed in MAFBs, which reduces the overall size and increases energy density indirectly. Third, an ion exchange membrane is usually indispensable for separating the anolyte and catholyte in RFBs.[69–73] While in MAFBs, except for some alkaline metal-based MAFBs with dual electrolytes, the electrolyte membranes are used for separating the metal and air electrodes and sometimes are even unnecessary,[74,75] which reduces the cost and eliminates the performance degradation caused by the transport resistance through the membrane.

In recent years, plenty of works about static MABs (e.g., LABs, ZABs) and battery components (metal electrode, electrolyte, air electrode) have been reported.[34,76–79] In addition, the reviews of static MABs have also been summarized by researchers.[75,80,81] By contrast, the work about MAFBs is still in its infancy, and few researchers have systematically reported the progress, challenges, and perspectives of MAFBs. Recently, the works about MAFBs are synoptically summarized in a review which gives an introduction of next-generation flow-battery technologies.[82] More recently, a review from the perspectives of material and chemistry was reported, which introduced the developments of vanadium-air flow batteries (VAFBs), zinc-air flow batteries (ZAFBs), and lithium-air flow batteries

View Article Online
DOI: 10.1039/C9TA10658H

(LAFBs) under both static and flow conditions.[83] It is worth noting that VAFBs should not be classified as the conventional MABs due to the application of vanadium ions of different valences (V^{3+}/V^{2+}) as redox couples instead of pure vanadium metal for the negative electrode reaction. In addition, the existing problems in ZAFBs and LAFBs have commonality and individuality since both kinds of batteries can be employed using either aqueous or non-aqueous electrolytes, making the division of MAFBs unreasonable only in light of the used metal. Moreover, although the developments of materials and structures of MAFBs were comprehensively overviewed, new issues of introducing the flow system are not emphasized specifically. Therefore, it is essential to summarize the previous works of MAFBs and offer new insights for further developments and practical applications, especially on the structural designs and the advances in materials.

We will start with a brief introduction to the system configurations and working principles, then discuss the flow media used in various systems and the classifications, MAFBs are divided into three categories according to structure features, working principles, and applications. Subsequently, the developments of MAFBs based on aqueous electrolytes will be presented in Section Three, including the advances in the metal and air electrodes. In Section Four, the achievements and problems of MAFBs based on non-aqueous electrolytes are discussed. Finally, the current status and the critical challenges of MAFBs are highlighted, along with the perspectives for further developments.

View Article Online
DOI: 10.1039/C9TA10658H

2. Battery configuration and working mechanisms

Different from VRFBs, the reactants of MAFBs are solid metals (on the metal electrode) and gaseous oxygen (on the air electrode) in discharge. Therefore, battery configurations and working mechanisms are substantially different. A lot of developments on MAFBs have been reported, and different kinds of solvents have been used depending on the nature of the metal, including aqueous and non-aqueous electrolytes. While in a specific MAFB, different types of electrolytes can co-exist with different flow forms. Thus, according to the electrolytes used and the flowing forms, the existing MAFBs can be loosely classified into three categories: one flow medium with one circulation, two flow media with one circulation, and two flow media with two circulations, which will be discussed in detail in this section.

2.1 One medium with one circulation

Commonly, conventional MABs are composed of three parts, a metal electrode, a porous air electrode, and an electrolyte. The metal electrode acts as the negative electrode and provide reactants while the air electrode provides reaction sites for the ORR and OER. As for MAFBs, the flow system is introduced to conventional MABs. Therefore, two external devices are needed, including a tank to store electrolyte and a pump to provide the flowing power. As schematically shown in Fig. 1, this type of MAFBs has similar components to those of static MABs except for employing an additional flow system to enable the circulation of the applied electrolyte in the whole battery during operation. To couple with the metal electrodes, different kinds of

View Article Online
DOI: 10.1039/C9TA10658H

electrolytes are applied.[84,85] For example, aqueous electrolytes are usually used in zinc-based flow batteries,[74] while non-aqueous electrolytes are generally employed for active metals (e.g., Li, Na).[34] In such kinds of MAFBs, only one kind of electrolyte is applied, and the ones with two or more electrolytes will be introduced latter.[86–88] Since the working principles are different when different types of electrolytes are used, the configurations based on aqueous and non-aqueous electrolytes are discussed separately.

For MAFBs with the flowing aqueous electrolytes, they can be mainly divided into two classifications. One is that the metal particles are added into the electrolyte to form a slurry, which circulates inside the negative region of the battery. As schemed in Fig. 1a, the aqueous electrolyte with metal particles (e.g., zinc pellets) is stored in a tank,[89] and the negative electrode only provides a place for the reactions of metal dissolution and precipitation. Taking the ZAFB as an example, the reactions on the negative electrode can be expressed as:

$$Zn + 4OH^- \underset{\text{charge}}{\overset{\text{discharge}}{\rightleftharpoons}} Zn(OH)_4^{2-} + 2e^- \quad (1)$$

During the discharge process, the mixtures of zinc particles and electrolyte driven by a pump are delivered to the negative electrode, and zinc particles are oxidized to divalent zinc ions (Zn^{2+}), combined with hydroxide (OH^-) to form Zn(OH)2− 4 and dissolved in the electrolyte. The electrochemical reactions on the positive (air) electrode are conventional ORR and OER processes during discharge and charge, respectively. For aqueous electrolytes, the ORR and OER are very complicated reactions and reaction kinetics are pretty sluggish. For the ORR, there exist two the

View Article Online
DOI: 10.1039/C9TA10658H

reaction pathways, two-electron pathway and four-electron pathway, when applying different catalysts and electronic structures.[90–92] The pathways of OER are the same complicated, which are different from ORR. Therefore, bifunctional catalyst is needed to accelerate the reaction rates of both ORR and OER. The reaction equation can be described as:

$$O_2 + 2H_2O + 4e^- \underset{\text{charge}}{\overset{\text{discharge}}{\rightleftharpoons}} 4OH^- \quad (2)$$

The combination of Reactions 1 and 2 results in the overall reaction:

$$2Zn + O_2 + 2H_2O + 4OH^- \underset{\text{charge}}{\overset{\text{discharge}}{\rightleftharpoons}} 2Zn(OH)_4^{2-} \quad (3)$$

Unlike a conventional Zn battery, the negative electrode of a MAFB acts only as a current collector so that dendrite formation and surface passivation are avoided. For this cell configuration, the critical challenge is how to fully utilized the metal particle in the electrochemical reaction and avoid the blockage of zinc particles in the electrode. It is worth mentioning that the cells with this configuration are recharged mechanically, which means that the zinc particles are fed mechanically and the aged electrolyte will be replaced by new one after a period of operation. Therefore, the reduction of zinc ions does not occur inside the battery.

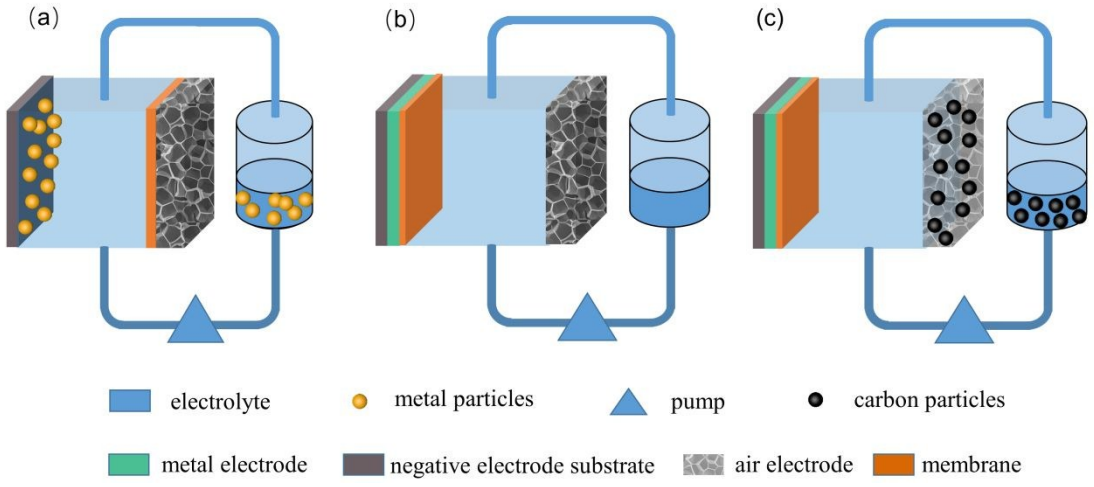

View Article Online
DOI: 10.1039/C9TA10658H

Fig. 1 Structure diagrams of MAFBs with one medium with one circulation. (a) metal particle slurries flow. (b) only the electrolyte flow. (c) carbon slurries flow.

The other one is that only the electrolyte acts as the flow medium. As schematically shown in Fig. 1b, the electrolytes are stored separately in an external tank that is connected to the battery through a pipe. In the discharge and the charge processes, the electrolyte forms a stable circulation between the positive electrode region of the battery and the tank under the action of a pump. The air electrode is usually made of porous materials (e.g., carbon paper, metal foam) to increase the reaction area,[80,93] while the negative electrode usually consists of metals in the form of foils or particles deposited on a substrate. For static ZABs, during the discharge process, when the concentration of $Zn(OH)_4^{2-}$ is high or even saturated, the formation rate of zinc oxide (ZnO) increases sharply,[94,95] which is a white flocculent precipitate and not electrically conductive. Due to the accumulation of ZnO on the negative electrode, the surface area in contact with the electrolyte is reduced, leading to the passivation.[79,96,97] Besides, the sluggish reaction kinetics of the ORR accompanying with the high species transport resistance greatly affect the electrochemical performance. After introducing the flow system, the generated $Zn(OH)_4^{2-}$ ions can be brought to the outside of the battery by the flow of the electrolyte, together with ZnO (if any), suppressing the passivation.[98–101] Additionally, species transport is accelerated, reducing the concentration polarization.[102,103] During the charge process, driven by the pump, the electrolyte containing $Zn(OH)_4^{2-}$ ions is sent to the battery to participate in the reaction. Different from the situation in the

View Article Online
DOI: 10.1039/C9TA10658H

static batteries where the formation of dendrite may occur, the flow of the electrolyte can shape the form of deposited zinc to inhibit the dendrite formation.[83,104] In addition, the generated oxygen (especially gaseous oxygen) during the OER can be taken out of the battery in time instead of occupying the porous electrode, avoiding the decrease of reaction sites and the leakage of the electrolyte caused by the high inner pressure.[83] The configuration shown in Fig. 1b can also be applied to batteries based on non-aqueous electrolytes such as lithium-air and sodium-air flow batteries.[105] The reactions for non-aqueous LAFBs can be expressed as follows:

Positive electrode:

$$2Li^{+}+O_2+2e^{-} \underset{\text{charge}}{\overset{\text{discharge}}{\rightleftharpoons}} Li_2O_2 \quad (4)$$

Negative electrode:

$$Li \underset{\text{charege}}{\overset{\text{discharge}}{\rightleftharpoons}} Li^{+}+e^{-} \quad (5)$$

Overall reaction:

$$2Li+O_2 \underset{\text{charge}}{\overset{\text{discharge}}{\rightleftharpoons}} Li_2O_2 \quad (6)$$

which are immensely different from those of ZAFBs. During the discharge process, lithium is oxidized to lithium ions (Li^{+}) and gradually dissolved in the electrolyte. Simultaneously, the ORR is carried out on the positive electrode. Because of the infiltration of the non-aqueous electrolyte,[74] oxygen first dissolves into the electrolyte to form dissolved oxygen, and then reduces to form super oxygen ions (O^{-}_2) and combines with Li^{+} transferred from the negative electrode to form lithium peroxide (Li_2O_2). Li_2O_2 does not dissolve in the non-aqueous electrolyte, reducing the active surface area and species transport pathways of the porous air electrode in static LABs.

View Article Online
DOI: 10.1039/C9TA10658H

Fortunately, its precipitation can be carried outside the battery accompanied by the flow of the electrolyte, which suppresses the above issues effectively.[105] During the charge process, the limited interfaces between the solid Li_2O_2 and the electrode and electrolyte hinder the deposition, resulting in a high overpotential. While carried by the circulating medium, the flowing electrolyte can accelerate the transport of ions and even carry solid Li_2O_2 to the porous air electrode to increase the contact interfaces, and thus facilitates the OER. In addition, the dendrite growth during the lithium deposition can also be mitigated by the flow of the electrolyte. Notably, lithium metal has strong reducibility and can react with many substances including the air electrode reactant, oxygen. Therefore, oxygen crossover is a very severe problem in LAFBs as the flow electrolyte enhances the oxygen transfer. Oxygen crossover can lead to various decomposition reactions and the corrosion of the lithium electrode.[106,107] Commonly, a ceramic membrane (Fig. 1b) is used to block oxygen crossover, as well as nitrogen and carbon dioxide.[34,107]

Inspired by ZAFBs with zinc particles flow, a semi-solid-flow LAB has been developed, as schematically shown in Fig. 1c.[108] This structure uses a semi-solid catholyte to circulate in the air electrode region of the battery, which is composed of carbon particles suspended in a non-aqueous electrolyte. By employing this semi-solid-flow design, the ORR and OER are carried out on carbon particles instead of the conventional porous air electrode, solving the clog and passivation issues. The details of this semi-solid-flow design will be introduced in the latter section.

View Article Online
DOI: 10.1039/C9TA10658H

2.2 Two media with one circulation

Generally, the discharge current densities of non-aqueous LABs are only about 0.1-1 mA cm^{-2}, far lower than those of ZABs (e.g., 10 mA cm^{-2}).[31] An important reason is the lack of gas phase caused by the complete saturation of non-aqueous electrolytes in the air electrodes.[109] Owing to the low oxygen dissolution rate, solubility, and diffusivity in common non-aqueous electrolytes, the oxygen concentration at the reaction interface is greatly limited. To solve this issue, hybrid electrolytes have been applied, which include two different types of electrolytes for the negative and positive electrodes, respectively as shown in Fig. 2a. Commonly, solid membranes are necessary to protect the lithium electrode. However, some of them (e.g., LATP: $Li_{1+x}Al_xTi_{2-x}(PO_4)_3$) will react with lithium.[110] Even for those that are stable when directly contacting with lithium (e.g., LAGP: $Li_{1+x}Al_xGe_{2-x}(PO_4)_3$), the interface resistance is large .[111] To this end, non-aqueous electrolytes are essential for this kind of configuration to protect lithium, increase the contact areas, and facilitate the transport of Li^+ ions. On the air electrode region, the aqueous electrolyte is applied to create more triple-phase boundaries for fast oxygen transport and solving the pore clog issue due to the formation of soluble discharge products (e.g., LiOH). To protect the metal electrode from aqueous electrolytes, the dual electrolytes are separated by a solid membrane that only allows the transport of Li^+ ions.

Stemmed from this concept, LAFBs with dual electrolytes in which only the catholyte is flowing have been proposed.[87,88] Fig. 2b shows a schematic diagram of the structure and working principle of a LAFB developed by He and co-workers.[87]

DOI: 10.1039/C9TA10658H

The non-aqueous and aqueous electrolytes are isolated by a Li^+-ion conducting glass-ceramic (e.g., LISICON) membrane. During discharge, lithium metal is oxidized to Li^+ ions as indicated in Reaction 5, which then transport through the solid membrane; while oxygen passes through the gas diffusion layer and reacts at the triple-phase boundaries based on Reaction 2. Since the degradation of the LISICON membrane occurs in a strongly alkaline condition, a cation exchange membrane is used to divide the aqueous electrolytes with different alkalinity to enhance the stability. At a current density of 0.5 mA cm^{-2}, the battery delivers a stable voltage of ~2.8 V and a high electrode capacity of ~19,000 mAh g−1 catalyst. At a lower current density of 0.1 mA cm^{-2}, the discharge voltage can reach ~3.2 V. When testing the battery performance with a higher current density of 1 mA cm^{-2}, the voltage maintains ~2.6 V, which is a manifest improvement in comparison with that of static LABs. Later on, Chen et al. made some optimizations to form a new type of hybrid LAFB.[88] The battery also consists of an electrochemical reaction unit and a recycling unit. While different from the structure in Fig. 2b, the electrochemical unit employs a relatively closed system in which the whole air electrode is immersed in the aqueous electrolyte completely. During discharge, gaseous oxygen is continuously introduced into the tank to dissolve in the electrolyte. By this method, the circulating aqueous electrolyte contains saturated oxygen without the requirement of oxygen from the gas diffusion layer, greatly reducing the transport resistance. In addition, a thicker air electrode can be applied, providing a larger reactive surface to enhance the reaction kinetics. At a current density of 1 mA cm^{-2}, the discharge and charge voltages are

View Article Online
DOI: 10.1039/C9TA10658H

stabilized at 3.2 V and 3.9 V, respectively, better than those of conventional LABs. At a high current density of 5 mA cm^{-2}, the discharge voltage maintains at 1.5 V, and a high power density up to 7.64 mW cm^{-2} is achieved at 4 mA cm^{-2}. Moreover, the resistance of the total battery is found to be determined by the Li^+-ion conducting glass-ceramic membrane, and its impedance should be reduced to effectively improve the battery performance.

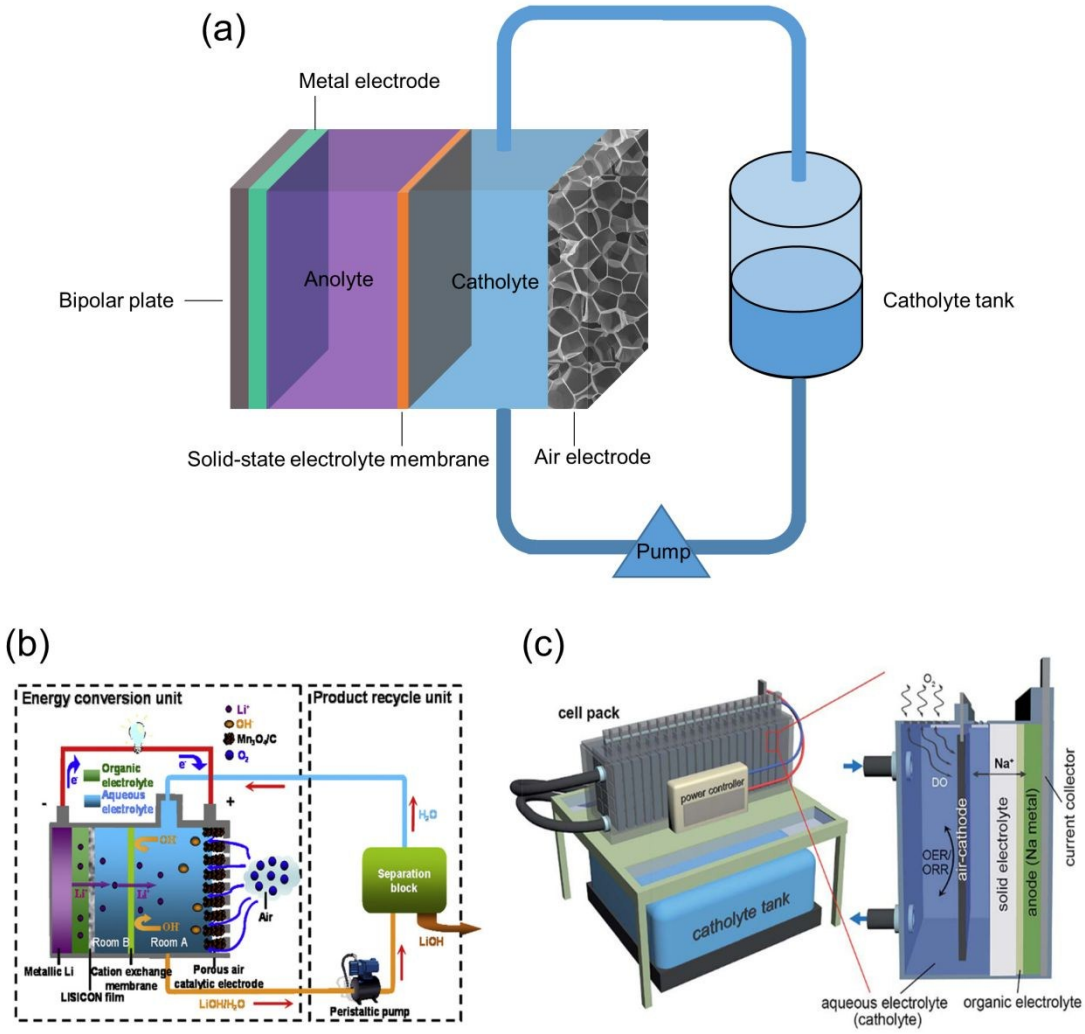

Fig. 2 (a) Structure diagrams of MAFBs with two media and one circulation. (b) A diagram showing the operational principle and configuration of the lithium-air flow battery. Reprinted with

View Article Online
DOI: 10.1039/C9TA10658H

permission from ref. 87. Copyright 2010, Elsevier. (c) Schematic illustration of the hybrid sodium-air flow battery equipped with a catholyte tank. Reprinted with permission from ref. 86. Copyright 2017, The Royal Society of Chemistry.

In addition to LAFBs, this flow structure can also be applied in MAFBs made of more reactive metals, such as sodium. A sodium-air flow battery with hybrid electrolytes (Fig. 2c) has been developed by Hwang and his co-workers.[86] This battery consists of the sodium metal electrode in a non-aqueous electrolyte and the air electrode in an aqueous electrolyte, which is separated by a Na^+-ion conducting glass-ceramic (e.g., NASICON) membrane. The aqueous catholyte is circulated in a flow-through mode, continuously replacing the reaction products with fresh reactants near the air electrode and helping convert ambient oxygen gases to dissolved oxygen in the catholyte. At a current density of 0.1 mA cm^{-2}, charge and discharge voltages of 3.68 V and 3.32 V with a peak power density of ~5.4 mW cm^{-2} are achieved, respectively. In addition, the battery shows good stability, and the voltage fluctuation is only 0.36 V in 20 cycles with a duration of 200 h.

2.3 Two media with two circulations

Besides the above-mentioned flow configurations, Wen et al. proposed a novel concept of a ZAFB based on two hybrid flow electrolytes by introducing a new substance, propanol, as a reactant to participate in an extra electrode reaction during charge.[99] As shown in Fig. 3a, this battery consists of two independent flow systems and an energy conversion unit. In the energy conversion unit, three electrodes divide

View Article Online
DOI: 10.1039/C9TA10658H

the unit into two parts for charge and discharge, respectively. During charge, the reactions on the positive electrode could be presented as follows:

$$2Ni(OH)_2 + 2OH^- \longrightarrow 2NiOOH + 2H_2O + 2e^- \quad (7)$$

$$CH_3CH_2OH + 4NiOOH + H_2O \longrightarrow CH_3CH_2COOH + 4Ni(OH)_2 \quad (8)$$

$$CH_3CH_2COOH + KOH \longrightarrow CH_3CH_2COOK + H_2O \quad (9)$$

The nickel hydroxide ($Ni(OH)_2$) on the electrode first reacts with the hydroxide ions in the electrolyte. Then, the product NiOOH reacts with propanol to regenerate $Ni(OH)_2$, maintaining its mass in the whole process. However, propanol will become propionic acid, which further reacts with KOH in the alkaline electrolyte, indicating that propanol is consumed throughout the process. The deposition of zinc occurs on the negative electrode as conventional ZABs (Reaction 1). The positive and negative electrodes are separated by an ion exchange membrane, and the propanol only circulates in the positive electrode side. Therefore, the OER is replaced by another reaction. During discharge, the porous air electrode and the metal electrode form a general ZAFB with the circulations of aqueous electrolytes and the reactions are the same as reaction 1 and reaction 2 in Section 2.1. To introduce air to the reaction zone, a "gas-introducing" structure was developed (Fig. 3a), which was further optimized into a "cavity-opening" structure to increase the oxygen transport rate (Fig. 3b). Consequently, the discharge voltage increases by about 100 mV, and the energy efficiency reaches up to 59.2%. Apparently, the introduction of propanol avoids the

View Article Online
DOI: 10.1039/C9TA10658H

issues during the OER, but results in a more complex battery structure.

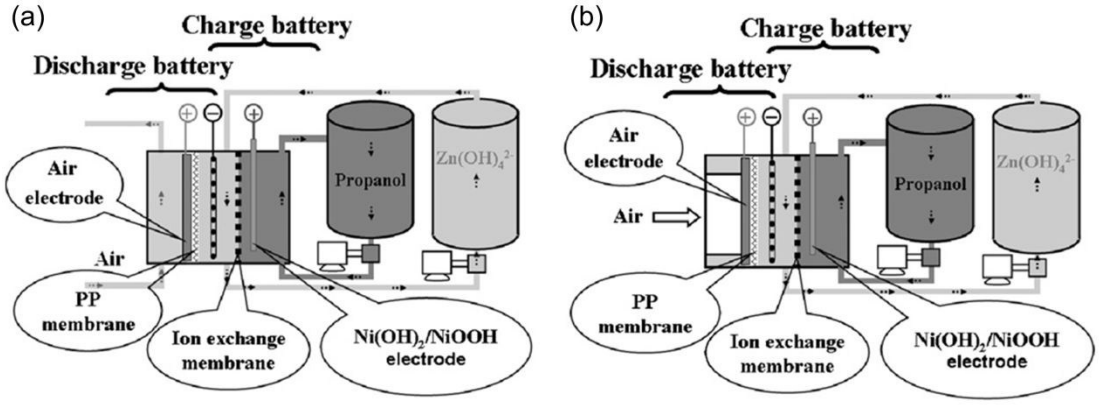

Fig. 3 The configuration of a ZAFB with two flow systems with the configuration of (a) a gas-introducing and (b) a cavity-opening structure. Reproduced with permission from ref. 99. Copyright 2009, Elsevier.

Recently, Brandon et al. reported a primary aluminum-air battery employing an oil flow displacement to suppress the open-circuit corrosion of the aluminum electrode.[112] The battery is divided into two parts by a separator with properties of oleophobicity and hydrophilicity. The air electrode side is full of the NaOH solution while the aluminum electrode side is supplied with the NaOH solution during operation and the insulating oil during standby respectively. During discharge, the electrolyte is continuously circulated inside the whole battery, but when the circuit is disconnected, the electrolyte in the aluminum side is replaced by the oil to suppress the open-circuit corrosion. During standby, the corrosion current density with this kind of flow structure maintains between 0.0001 to 0.0011 mA cm^{-2}, which is several orders of magnitude lower than that of the conventional battery (1 to 10 mA cm^{-2}). The battery delivers an energy density of 2.08 ± 0.07 Wh g−1 Al while the value

View Article Online
DOI: 10.1039/C9TA10658H

drops to 0.4 ± 0.07 Wh g−1 Al in the conventional battery in an intermittent test of 5 min operation at a current density of 150 mA cm^{-2} and 24- or 72-hour pauses. This work provides ideas for applying flow systems to address some issues that the static batteries can hardly handle.

3. Flow media based on aqueous electrolytes

MABs based on aqueous electrolytes usually include aluminum-air, magnesium-air, zinc-air, and some lithium/sodium-air batteries.[75,80,86,113,114] From Section Two, the basic reactions (OER and ORR) on the air electrodes of aqueous MAFBs are similar. Among aqueous MABs, the ones using magnesium and aluminum suffer from severe passivation and corrosion, which greatly hinder their electrochemical rechargeability and performance.[113,115–118] For the ones using lithium or sodium, the inevitable use of glass-ceramic membranes complicates the battery configuration, and the use of non-aqueous electrolytes, as well as the occasional contact of alkaline metals and the aqueous solvents, also threaten the safety. In contrast, ZABs have intrinsic safety and can be recharged electrochemically.[89,101,102,119–122] In this section, we will introduce the developments and common issues based on the battery components instead of the specific types. The metal electrode designs will be first summarized, followed by the air electrode designs. The electrochemical performance of different types of MAFBs will be also compared at the end of this section.

3.1 Metal electrode design

The metal electrodes are usually composed of metallic plates or powders deposited on

View Article Online
DOI: 10.1039/C9TA10658H

current collectors.[30,123] While during the repeated discharge and charge processes, some issues such as dendrite formation, hydrogen evolution, shape changes, and passivation, will decrease the utilization of the metal electrode, cause the capacity loss, limit the cycle life, and even lead to the short-circuit.[95,120,124–126] Many feasible approaches have been proposed to address these issues.[124,127–130] As one promising strategy, the surface coating is conducted by introducing a protective layer for the metal electrode, which can effectively suppress the dendrite formation, hydrogen evolution, and passivation. The introduction of additives is another way to enhance the performance of the metal electrode.[131,132] For example, the most commonly used additives for the zinc electrode include Bi_2O_3, $Ca(OH)_2$, PbO, SnO_2, and LiBO.[133] As most of the aqueous MAFBs focus on ZAFBs, we will take the zinc electrode as an example to discuss the effective design strategy.[83,97,121]

Since zinc particles and slurries are usually used, the corresponding metal electrode design is demanded to address the issues of zinc utilization, the blockage caused by remaining zinc, and solid products and by-products. The most common design employs a zinc electrode chamber with a tapered-end structure, as shown in Fig. 4a.[102,134,135] In the early time, Cooper et al. reported a zinc-air fuel cell employing tapered-end structure chamber as the negative electrode fed with zinc particle slurries.[135] During discharge, zinc particle slurries are pumped into the chamber through a hopper where the zinc particles are oxidized. The size of zinc particles gradually decreases during discharge, and thus zinc particles can automatically flow from the upper end to the lower end of the chamber. Based on this design, a fuel stack

View Article Online
DOI: 10.1039/C9TA10658H

was developed with the tapered-end structured chambers, in which zinc particles were fed by the gravity while the electrolyte was driven by the pump during discharge. As a result, a peak power density of 435 mW cm^{-2} was achieved. In addition to this design, two kinds of tapered-end structured chambers (type V and type Y) were tested to fully utilize the active areas, as shown in Fig. 4b.[102] The experimental results showed that the bottom portion of the type V chamber was not filled with zinc particles, causing a sharp decrease of the effective active area of the anode. In contrast, zinc particles filling the type Y chamber were much more homogeneous, and the inactive region was reduced to a minimum value. The peak power density with the type Y chamber was as high as 274 mW cm^{-2} at the current density of 420 mA cm^{-2}, while the value with the type V one was only 110 mW cm^{-2} at the current density of 123 mA cm^{-2} under the same operating condition. Apart from the tapered-end structure, a zinc electrode bed was also reported (Fig. 4c).[89] During discharge, zinc particle slurries are pumped into the bed and the zinc particles are trapped within the bed, while the electrolyte keeps flowing from the top to the bottom. As the dissolution of zinc particles, the size becomes smaller and then the particles migrate to the bottom of the bed. Using this design, a single battery could successfully operate for 1000 h, delivering a stable power density of 300 mW cm^{-2}.

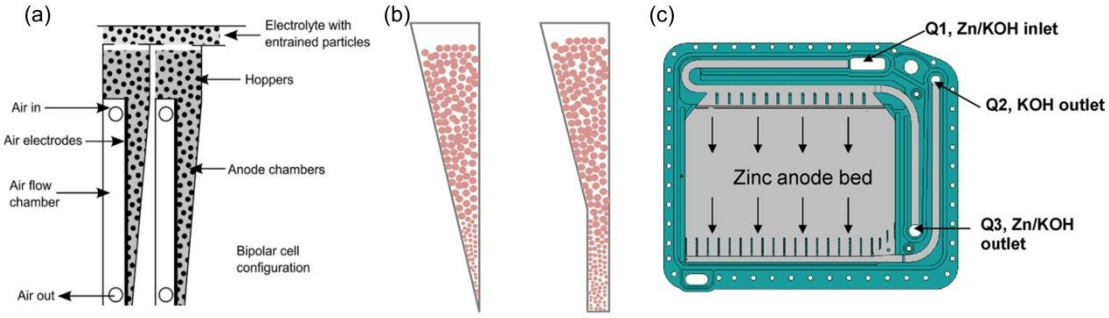

View Article Online
DOI: 10.1039/C9TA10658H

Fig. 4 (a) Negative electrode chamber with trapped-end structure. Reprinted with permission from ref. 26. Copyright 2015, Elsevier. (b) Anode chamber with trapped-end structure: type V (left) and type Y (right). Reprinted with permission from ref. 102. Copyright 2014, Elsevier. (c) Zinc fuel cell frame with zinc bed structure. Reprinted with permission from ref. 89. Copyright 2007, Elsevier.

Passivation is considered to be another factor that limits the metal electrode performance. As the operating time goes by, the concentration of hydroxide ions in the solution gradually decreases, and conversely, the concentration of zincate ions ($Zn(OH)_4^{2-}$) slowly reaches to saturation, which will cause the precipitation of insoluble and insulating product zinc oxide (ZnO).[134,136] ZnO is difficult to be electrochemically reduced to zinc and is easy to adhere to the electrode surface, reducing the active surface area of the metal electrode.[96,97,133] Actually, the passivation phenomenon is not obvious in most reported ZABs since the concentration of zinc ions in the electrolyte is not saturated, and the rate of generating zinc oxide is relatively low for ordinary discharge. However, when the concentration of zinc ions in the electrolyte is saturated as occurred in the deep discharge case, the battery performance is largely affected.[134,136,137] Using flowing electrolyte or slurry is an effective approach to alleviate the surface passivation and enhance battery performance.[119,134] Puapattanakul et al. investigated the flow effects on zinc-air fuel cell performance by comparing the cells with static electrolyte, flowing electrolyte, and flowing gelled KOH electrolyte, respectively.[119] The results demonstrated that the average current of the cell with the flowing electrolyte was 27% higher than that with

View Article Online
DOI: 10.1039/C9TA10658H

the static electrolyte at a constant voltage of 0.7 V. Besides, the gelled KOH electrolyte provided no evident improvements on the battery performance but reduced the gas evolution and alleviated the zinc oxidation caused by hydroxide ions during discharge. To get in-depth information of the flow effects on the passivation, a flow zinc-air fuel cell was fabricated with a mechanically refuelable tapered-end zinc electrode chamber filled with zinc particles with an average diameter of 0.4 mm.[134] At a constant current of 212 mA, the capacity with the flowing electrolyte was one order of magnitude higher than that with the static electrolyte, and adding fresh electrolyte cannot improve the values due to the blockage caused by zinc particles. Thus, the suppression of on the passivation and the improvement of battery performance by using the flowing electrolyte were illustrated. A passive model on zinc particles with a ZnO shell was also proposed, as shown in Fig. 5a. At the initial discharge stage, the passivation is hindered due to the high concentration of hydroxide ions maintained by the flowing electrolyte. After long time discharge, the zincate concentration gradually reaches saturation and the concentration of hydroxide ions decreases, resulting in the passivation. Two kinds of passivation films (Fig. 5b) are proposed, including an inner light gray/black dense ZnO layer (type II) in the region closer to the anode surface at the metal/electrolyte interface in the lower pH condition and an external white porous layer (type I) by precipitation of saturated zincate ions ($Zn(OH)_4^{2-}$). Although the electrolyte storage tank provides a large amount of electrolyte for the cell and collects the products and by-products, a large space is demanded which decreases the energy density and in turn limits the commercial applications. To further optimize the cell

View Article Online
DOI: 10.1039/C9TA10658H

structure, a novel system with a filter instead of the electrolyte storage tank to isolate reaction product precipitations and suppress anode passivation was proposed by Pei and co-workers.[136] The filter made of titanium powder can effectively remove the ZnO from the electrolyte with the efficiency of nearly 100%. From the experimental results, the battery without a filter had a clear voltage decrease and white precipitation in the electrolyte, while the one with a filter could still operate with a stable voltage over 1.1 V and the solution remained transparent. Two flow fields with low (2300) and high (9200) Reynolds numbers were also employed, and the passivation layers on the electrode could be easily damaged in the higher Reynolds number condition. Recently, to suppress corrosion and passivation of zinc particles, functional electrolyte additive has been introduced to ZAFBs, such as ethanol.[138] Alkoxide ions, which originate from the transformation of alcohols in alkaline solutions, can compete with hydroxide ions for the coordination of Zn^{2+} ions.[139] Consequently, the introduction of ethanol can suppress the formation of ZnO, and the concentrations of 5–10% v/v ethanol was found to be beneficial for the dissolution and the hindrance of passivation. In addition, two kinds of surfactants have also been proposed, including sodium dodecyl sulfate (SDS) and Pluronic F-127 (P127).[98,140] The specific discharge capacity increments of 30% and 24% were achieved in the electrolyte containing 100 ppm P127 and 0.2 mM SDS, respectively.

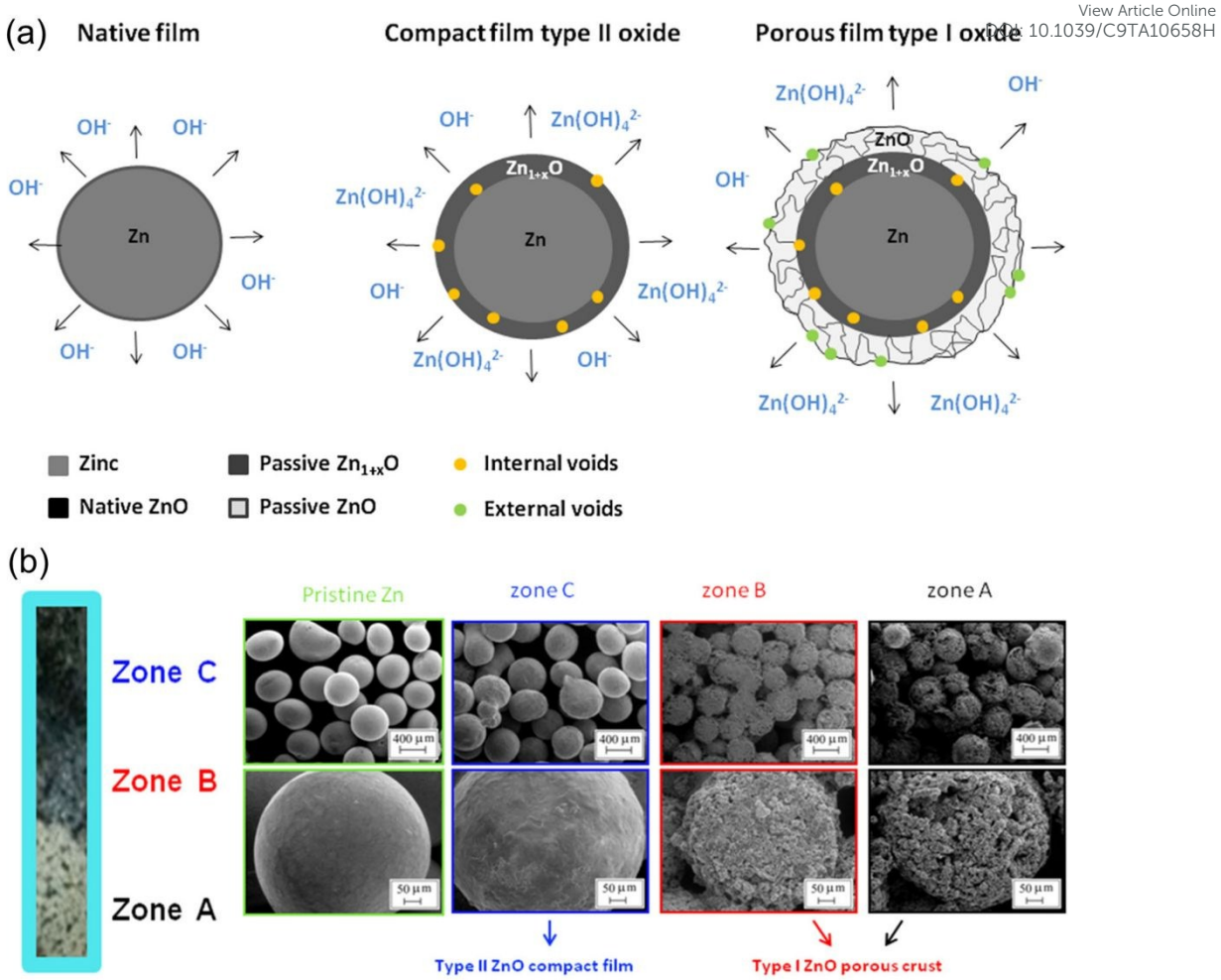

Fig. 5 (a) Model of spherical Zn particles with passive ZnO shell. (b) Physical images (left) and SEM micrographs at the magnifications of 100 × and 500× (right) of the passivation model. Reproduced with permission from ref. 134. Copyright 2017, Springer.

For electrically rechargeable metal-based batteries, dendrite is a key factor that restricts performance and safety. In alkaline solutions, zincate (Zn(OH)2– 4) is the main product in the discharge process, which should be completely reduced to zinc in the charge process. However, the concentration of zincate on the electrode surface is different from that in the electrolyte due to the transport resistant. As the electrode surface is not absolutely smooth, the concentration gradient makes the deposition rate non-uniform, resulting in the dendrite growth.[104,124] The influences of the flowing

View Article Online
DOI: 10.1039/C9TA10658H

electrolyte on the zinc deposition process have been investigated, which revealed that the circulation of the electrolyte can inhibit dendrite growth. Wang et al. established a three-dimensional model and conducted experiments to illustrate the morphology control of zinc regeneration in the presence of flow media.[104] As shown in Fig. 6a, the convection caused by flow media dominates the mass transport in the electrolyte rather than the diffusion, making the concentration of each part in the electrolyte uniform. With an increase of Peclet number (a dimensionless parameter to measure the proportion of convective transport and diffusion transport), the distribution of ion concentration in the electrolyte becomes more and more uniform. To get an insight view of the effects of flow media, the SEM images of the zinc morphology deposited under the static (up) and flow (down) conditions are presented in Fig. 6b, respectively. Apparently, the morphology under the flowing electrolyte is more compact than that under the static electrolyte. Hence, through reducing the concentration gradients between the surface of the zinc electrode and the bulk electrolyte, the flowing electrolyte can suppress dendrite growth effectively. It is worth noting that the effects on the dendrite suppression have been demonstrated in the plate-like metal electrode. For the new designs such as porous metal electrodes,[141] the incorporation of flowing electrolyte may further inhibit the dendrite and enable better cycling stability.

View Article Online
DOI: 10.1039/C9TA10658H

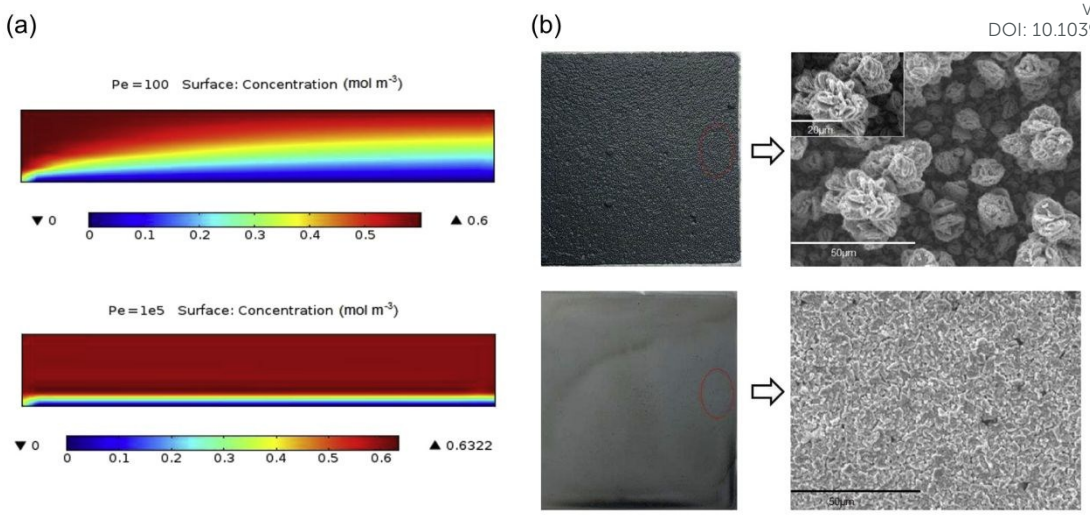

Fig. 6 (a) Electrolyte concentration: Pe =100 (up), and Pe = 1e5 (down). (b) Deposited zinc morphologies in weight 40% KOH with 1 M zinc oxide with electric quantity for 10 min at the current density of 100 mA cm^{-2}, of quiescent electrolyte (up), and flowing electrolyte (down). Reproduced with permission from ref. 104. Copyright 2014, Elsevier.

3.2 Air Electrode design

The air electrodes are mainly composed of a porous gas diffusion layer for oxygen transport and a catalyst layer for oxygen electrochemical reactions.[74,84,142] In aqueous MABs, during discharge, oxygen in ambient air passes through the gas diffusion layer to the triple-phase boundaries and then is reduced (ORR).[143] During charge, oxygen is evolved at the electrolyte/electrode interfaces (OER) and then releases to the air through the gas diffusion layer. Different from the metal electrode, the ORR and OER are mutually reversible processes, but the reaction paths and reaction processes are not completely reversible. The catalysts that have high activity for the ORR, unfortunately, are usually suffering from the insufficient activity for the OER. When introducing the flow media to the static MABs, the mass transport (e.g., ions, oxygen,

View Article Online
DOI: 10.1039/C9TA10658H

products, and by-products) can be enhanced,[83] while developing effective catalysts and optimizing electrode structures are still essential for MAFBs.

3.2.1 Decoupled electrodes

The design of decoupled electrodes means that the battery has two positive electrodes for charge and discharge processes, respectively, in which two catalysts for the ORR and OER are employed, respectively.[74,123] Bockelmann et al. reported a ZAFB applied a three-electrode design, as shown in Fig. 7a.[120] Two commercial positive electrodes were used, including a silver electrode for the ORR and a nickel foam electrode for the OER. At a dramatically high current density of 600 mA cm^{-2}, the battery still delivered a discharge voltage of 0.4 V and a charge voltage of 2.7 V with 14.8% voltage efficiency (Fig. 7b). At a lower current density of 460 mA cm^{-2}, the peak power density reached 270 mW cm^{-2}. Besides, the influence of operating temperature on the performance was also investigated (Fig. 7c). With an increase of operating temperature from 22 to 40 ^{o}C, the voltage efficiency raised slightly from 58% to 61%, but the cyclability of the battery declined dramatically. Moreover, the battery operated stably in 250 cycles at the current density of 50 mA cm^{-2}, and a longer cyclability of 600 cycles (Fig. 7d) was achieved after solving the dendritic connection on the zinc electrode. In addition to the single battery, the three-electrode system has also been applied to the stack. Amunátegui et al. built a stack of twenty tandem ZAFBs in which the single battery consists of three electrodes.[144] The prototype consists of three different stacks connected in parallel, each of which is composed of 20 single cells

View Article Online
DOI: 10.1039/C9TA10658H

connected in series and 0.25 m^3 of electrolyte, delivering 1.8 kWh at medium power (0.5 kW) and 3.0 kWh at low power (0.24 kW). At a current density of 25 mA cm^{-2}, 2000 discharge-charge cycles were tested. In the beginning, the energy efficiency and coulombic efficiency achieved 48% and 82%, respectively, while the values decreased to 34% and 69%, respectively, due to gas diffusion layer flooding, zinc accumulation, and short-circuits. Although the three-electrode design can address the problem of different catalyst requirements for the ORR and OER, it is not a perfect design owing to its cost and complexity, which not only complicates the internal structure of the battery but also increases the requirements for external circuits.

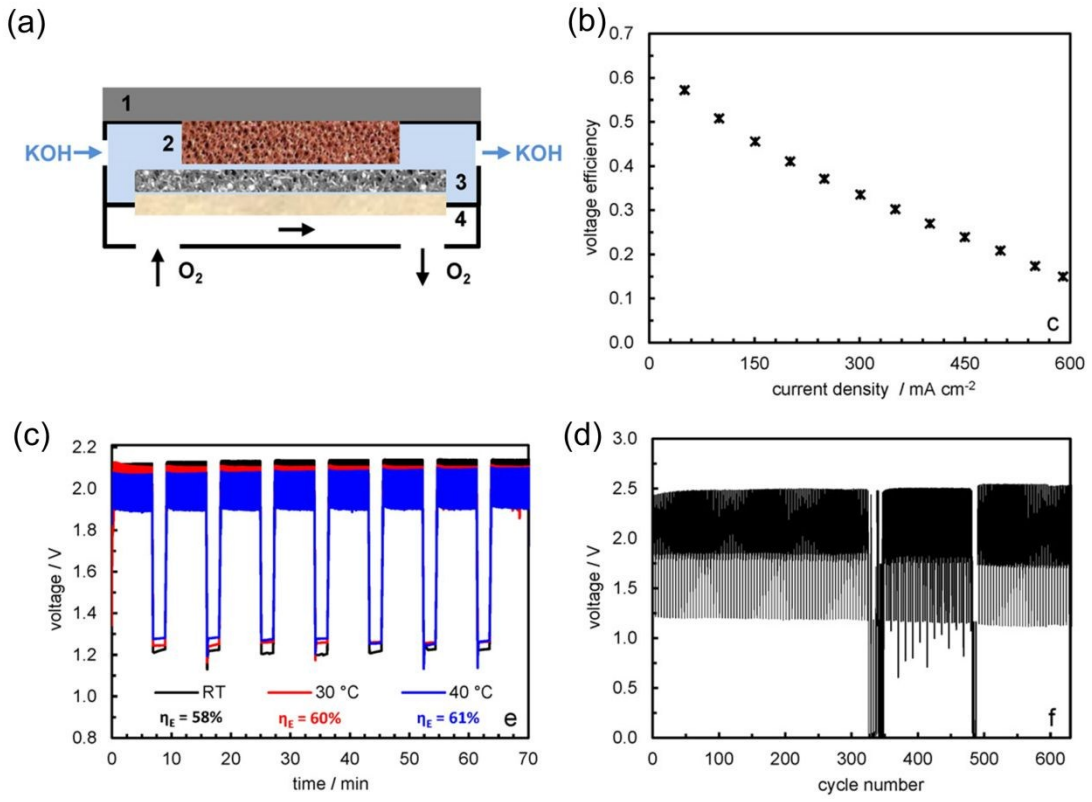

Fig. 7 (a) Schematic illustration of the testing cell: (1) zinc plate, (2) copper foam, (3) nickel foam, (4) oxygen depolarized cathode. Characteristics of electrically rechargeable zinc-oxygen cell: (b) voltage efficiency as a function of current density, (c) influence of operating temperature on cell

View Article Online
DOI: 10.1039/C9TA10658H

performance at 50 mA cm^{-2}, (d) cyclic performance of the cell over 600 cycles at room temperature (22 °C) and 50 mA cm^{-2}. Reproduced with permission from ref. 120. Copyright 2016, Elsevier.

3.2.2 One electrode with bifunctional catalysts

Compared to the three electrode design, the two-electrode design is preferred due to the simple and compact structure. The basic approach is to integrate two highly efficient catalysts that are responsible for the ORR and OER onto the air electrode. Pan et al. reported a ZAFB employing nano-structured $Ni(OH)_2$ and electrolytic MnO_2 doped with $NaBiO_3$ as the highly-efficient catalysts for the OER and ORR, respectively (Fig. 8a).[121] This battery delivered average coulombic efficiency of 97.4% and energy efficiency of 72.2% in 150 cycles (Fig. 8b). Apart from transition metal oxide catalysts, perovskites and spinels are widely used in ZABs in recent years. The mixture of $La_{0.6}Sr_{0.4}Co_{0.2}Fe_{0.8}O_3$ perovskite and $NiCoO_4$ spinel have been applied in ZAFBs.[122,145,146] At a current density of 50 mA cm^{-2}, the battery with $La_{0.6}Sr_{0.4}Co_{0.2}Fe_{0.8}O_3$ perovskite and $NiCoO_4$ spinel bi-catalyzed bifunctional air electrode operated stably for 1000 h and 450 cycles in pure oxygen condition and over 650 h and 300 cycles in synthetic air condition (80% N_2/20% O_2), respectively.

The use of two kinds of catalysts will inevitably increase the cost and complexity. Thus, developing bifunctional catalysts with activity for both ORR and OER is significant.[80,147–150] Till now, plenty of bifunctional catalysts have been reported and applied in MAFBs. A bifunctional air electrode employing $La_{0.6}Sr_{0.4}Co_{0.2}Fe_{0.8}O_3$ perovskite and an optimized amount of polytetrafluoroethylene (PTFE) and carbon

View Article Online
DOI: 10.1039/C9TA10658H

nanofibers (CNFs) was reported by Pichler and his co-workers.[101] PTFE acts as a hydrophobic binder material and CNFs benefit for the oxygen transport and electrical conductivity by forming a fibrous electrically conductive network. A ZAFB with this electrode demonstrated dramatically high stability for over 1800 h. Meanwhile, stable operation with the voltage efficiency of higher than 50% was achieved in 1000 h. Carbon-based materials with heterogeneous atoms doping as bifunctional catalysts have attracted increasing attention in the past several years.[150–152] Recently, a hybrid catalyst composed of interpenetrating Co and Co_3O_4 nanoparticles stitched in a porous graphitized shell (Co/Co_3O_4@PGS) was developed as a bifunctional catalyst for ZAFBs.[153] This bifunctional catalyst achieved better performance than the precious metal and oxide catalysts, as shown in Fig. 8c and 8d. The battery with Co/Co_3O_4@PGS demonstrated a lower over-potential and a higher power density of 118.27 mW cm^{-2}, delivering high cyclability for 800 h (4800 cycles) at a current density of 10 mA cm^{-2}. More recently, Guo et al. reported a novel and excellent bifunctional electrocatalyst made of a metallic Fe-Ni alloy encased in nitrogen-doped carbon based on predesigned covalent organic polymers ($CCOP_{TDP}$–FeNi–SiO_2) for a ZAFB, which delivered a peak power density of 112.8 mW cm^{-2} and lower charge-discharge voltage gaps of 0.79 V and 1.24 V at 5 mA cm^{-2} and 20 mA cm^{-2}, respectively.[154]

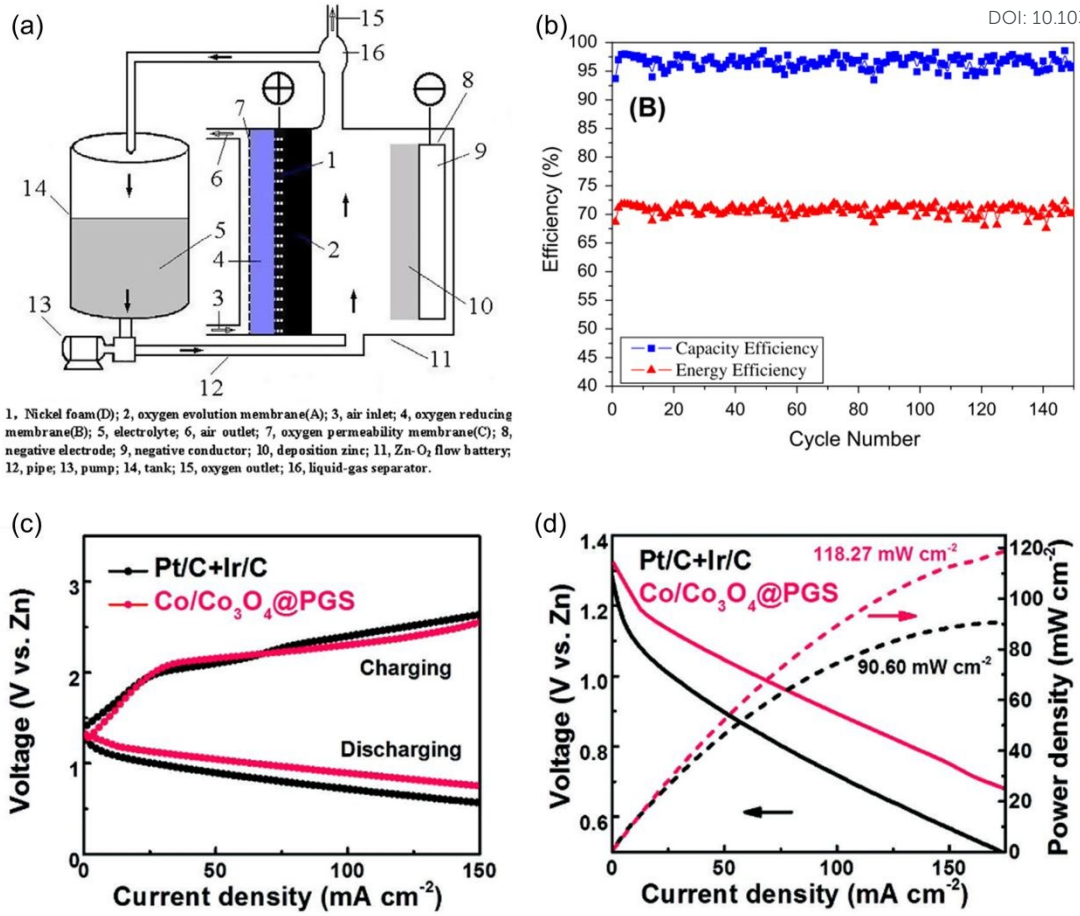

Fig. 8 (a) Schematic diagram and (b) coulombic efficiency/energy efficiency curves in the first 150 cycles of the single flow Zn–O_2 battery with a bifunctional air electrode. Reproduced with permission from ref. 121. Copyright 2009, Elsevier. (c) Charge and discharge polarization curves, and (d) discharge polarization curves and the corresponding power density plots for Zn–air battery with Co/Co_3O_4@PGS and Pt/C+Ir/C catalysts. Reproduced with permission from ref. 153. Copyright 2018, Wiley Online Library.

3.3 Performance comparisons

Table 1 Performance comparison of MAFBs based on aqueous electrolytes.

Metal electrode	Air electrode	Electrolyte	Recharge method	Electrochemical performance	Ref
Zinc particles with zinc	Platinum catalyst	45 wt.% KOH	Mechanical	Power density: 300 mW cm^{-2} Cyclability: 1000 h at constant power density of 300 mW cm^{-2}	[89]

View Article Online
DOI: 10.1039/C9TA10658H

trapped bed					
Zinc particles with trapped end chamber	MnO_2 catalyst	40 wt.% KOH	Mechanical	Peak power density: 435 mW cm^{-2} Operational current density: 510 mA cm^{-2}	[102]
zinc powder	MnO_2 catalyst	8 M KOH	Mechanical	Peak power density: 240 mW cm^{-2}	[103]
Zinc particles with trapped end chamber		6 M KOH	Mechanical	Peak power density: 36 mW cm^{-2} Specific capacity: >770 mAh g−1 Zn Energy density: >894 Wh kg−1 Zn	[134]
Zinc particles	MnO_2 catalyst	8 M KOH with ethanol as an additive	Mechanical	Peak power density: >32 mW cm^{-2} Specific capacity: 470 mAh g−1 Zn Energy density: 576 mWh g−1 Zn	[138]
Zinc particles		7 M KOH with surfactants	Mechanical	Peak power density: >78 mW cm^{-2} Specific capacity: 350 mAh g−1 Zn Energy density: 360 mWh g−1 Zn	[140]
Zinc foil		30 wt.% KOH	Mechanical	Electrolyte capacity: 1025 Ah L^{-1}	[136]
Deposited zinc	$Ni(OH)_2$ and MnO_2 doped with $NaBiO_3$	7 M KOH with 0.7M LiOH and 0.7M ZnO	Electrochemical	Coulombic efficiency: 97.4% Energy efficiency: 72.2% Cyclability: 150 cycles at 20 mA cm^{-2}	[121]
Zinc foil	$NiCo_2O_4$ spinel and $La_{0.6}Sr_{0.4}Co_{0.2}Fe_{0.8}O_3$ perovskite	8 M KOH with 0.5 M ZnO	Electrochemical	Voltage efficiency: 62% Cyclability: 1000 h and 450 cycles at 50 mA cm^{-2}	[145]
Deposited zinc	$NiCo_2O_4$ spinel and $La_{0.6}Sr_{0.4}Co_{0.2}Fe_{0.8}O_3$ perovskite	8.0 M KOH and 0.5 M ZnO	Electrochemical	Energy efficiency: 49% Cyclability: 450 h and 200 cycles at 50 mA cm^{-2}	[146]
	$NiCo_2O_4$ spinel and	8.0 M KOH and 0.5 M	Electrochem	Cyclability: 1820 h at 50 mA cm^{-2}	[101]

View Article Online
DOI: 10.1039/C9TA10658H

Zn plate	$La_{0.6}Sr_{0.4}Co_{0.2}Fe_{0.8}O_3$ perovskite	ZnO	ical	Voltage efficiency: 57%	
Zinc foil	$NiCo_2O_4$ spinel and $La_{0.6}Sr_{0.4}Co_{0.2}Fe_{0.8}O_3$ perovskite	8.0 M KOH and 0.5 M ZnO	Electrochemical	Cyclability: 800 h at 50 mA cm^{-2} Voltage efficiency: 68%	[122]
Zinc plate	Co/Co_3O_4@PGS	6.0 M KOH	Electrochemical	Peak power density: >118.27 mW cm^{-2} Cyclability: 800 h and 4800 cycles at 10 mA cm^{-2} Voltage efficiency: 55% at 10 mA cm^{-2}	[153]
Zinc plate	$CCOP_{TDP}$–Fe Ni–SiO_2 catalyst	8.0 M KOH and 0.5 M ZnO	Electrochemical	Peak power density: 112.8 mW cm^{-2} Voltage efficiency: 59% at 5 mA cm^{-2}	[154]
Deposited zinc	Two positive electrode (a nickel electrode and a silver electrode)	30wt.% KOH electrolyte with 2 wt.% ZnO	Electrochemical	Peak power density: 270 mW cm^{-2} Cyclability: 600 cycles at 50 mA cm^{-2} Energy efficiency: 54%	[120]
Sodium plate	Pt/C and IrO2 catalysts	1 M NaNO3 and 0.1 M citric acid catholyte and a solid electrolyte (NASICON)	Electrochemical	Peak power density: 5.4 mW cm^{-2} Cyclability: 20 cycles and 200 h at 0.1 mA cm^{-2} Voltage efficiency: 89%	[86]
Lithium foil	Carbon nanofoam	0.85 M CH3COOH and CH3COOLi	Electrochemical	Peak power density: 7.64 mW cm^{-2} Cyclability: 20 cycles and 200 h at 0.1 mA cm^{-2} Voltage efficiency: 82%	[88]
Lithium metal	Mn_3O_4/ activated carbon composite	1M LiOH and $LiNO_3$	Mechanical	Peak power density: 1127W kg^{-1} Electrode capacity: 19000 mAh g−1 catalyst	[87]

Table 1 lists the compositions and performance of various MAFBs based on aqueous flowing electrolytes. ZAFBs occupy most of the works due to the advantages

View Article Online
DOI: 10.1039/C9TA10658H

mentioned at the beginning of this Section. In ZAFBs, two different charge methods, namely mechanical and electrochemical, are employed. For mechanically charged ZAFBs, a high power density (435 mW cm^{-2} for the highest) accompanied by stable and long-time operating under high current densities can be achieved.[102] In addition, dendrite growth can be fully avoided since no zinc deposition occurs inside the battery. However, the passivation is severe after the long-time operation, which is inevitable due to the saturated zincate ions. This can be addressed by replacing the aging electrolyte with a new one.[134] Besides, the low utilization and clog problems caused by zinc particles cannot be ignored during operation. For electrochemically charged ZAFBs, catalysts for the ORR and OER plays crucial roles in improving the power density, cycling stability, and energy efficiency. As the developments of materials, many bifunctional catalysts have been developed, which can highly improve the stability of long-term operation and demonstrate better performance over precious metal and metal oxide catalysts. However, the energy efficiency (about 70%) is still not very high for practical applications. It is worth mentioning that the areal power density varies so dramatically between different ZAFBs, which are mainly caused by the catalyst and recharging method applied to the batteries. Besides ZAFBs, lithium and sodium-air batteries using aqueous flowing electrolytes have also been developed by employing ceramic membranes to protect active metals.[87,155] Unfortunately, for LAFBs, although the power densities are ameliorated compared with the static LABs, the power densities are one to two orders of magnitude lower than those of aqueous ZAFBs, which may be caused by the high resistance of ceramic

View Article Online
DOI: 10.1039/C9TA10658H

membrane, parasitic reactions, and sluggish reaction rate caused by the lack of pathways for gaseous oxygen on the air electrode.[75] In addition, the cyclability is also below the requirements of practical applications. Considering the promising prospects, the battery materials (e.g., membrane and catalysts), structure designs (flow field and air electrode), and operating management (e.g., atmosphere and temperature) deserve deep investigations.

4. Flow media based on non-aqueous electrolytes

In MAFBs based on aqueous electrolytes, the mass transport (e.g., oxygen, ions) is enhanced and the electrochemical performance can be improved compared with the static ones. Especially for LAFBs based on aqueous flowing electrolytes, the product is changed from solid Li_2O_2 to soluble LiOH, avoiding the pore clog issue. However, shortcomings also exist. First, the solubility of LiOH is lower than that of KOH or NaOH, which can easily lead to product precipitation during the discharge process. Additionally, a lithium protected layer (e.g., LISICON plate) is demanded to avoid the direct contact between lithium and aqueous electrolytes,[88,156,157] which suffers from the insufficient stability in alkaline and/or acidic solutions and low ionic conductivity. Therefore, LAFBs based on non-aqueous electrolytes have also been proposed. In static LABs based on non-aqueous electrolytes, the high oxygen transport resistance and insoluble Li_2O_2 deposition are the main problems that affect the performance,[75,158,159] but these can be effectively alleviated through the circulating media.[83,160] Although non-aqueous electrolytes have been applied in various kinds of

View Article Online
DOI: 10.1039/C9TA10658H

MABs (e.g., lithium-air, sodium-air, potassium-air,[161] and even zinc-air batteries[74,162,163]), the reported non-aqueous MAFBs are still concentrated on LAFBs. Hence, we will overview the developments of LAFBs based on non-aqueous electrolytes in this section, focusing on the strategies to solving the inherent issues (e.g., poor cycle life, low real capacity).[164,165]

4.1 Mass transfer enhancement

4.1.1 Modeling works

Mathematical modeling can provide details in the batter operation that are difficult to measure and can serve as a power tool for design optimization. An immense amount of modeling works on the detailed process of static LABs have been conducted,[166] such as the lithium ion transport,[167–169] oxygen transport,[167,170,171] and deposition of Li_2O_2,[172,173] but the convection effects of the electrolyte are usually neglected. While for LAFBs, due to the influence of flow media, transport phenomena (e.g., oxygen, ions, insoluble products, and by-products) during charge and discharge change dramatically.[83] Hence, models for LAFBs need to be further optimized to fit the real conditions.

Based on the previous models of conventional redox flow batteries[174–178] and static non-aqueous LABs,[179–185] a two dimensional, transient, non-isothermal simulation model for LAFBs was reported to investigate the heat and mass transfer in the flow condition.[186] The air electrode was set to have internal flow channels, and two different pressures were employed in the inlet and outlet respectively to simulate

View Article Online
DOI: 10.1039/C9TA10658H

the circulation inside. As shown in Fig. 9a, the specific discharge capacity of the flow model is 1217 mAh g^{-1}, while the value dramatically decreases to 178 mAh g^{-1} in the static model at the discharge current density of 0.2 mA cm^{-2}. When increasing the discharge density to a higher value of 2 mA cm^{-2}, the discharge capacity of the flow model is about 15 times higher than that of the static model (201 mAh g^{-1} versus 12.2 mAh g^{-1}). This is because the flowing electrolyte can effectively enhance the mass transfer (especially oxygen transport) and improve the utilization of the air electrode. The volume fractions of the Li_2O_2 after discharge in flow and static models are compared, as shown in Fig. 9b. The horizontal axis (χ) of the graph is the dimensionless length of the air electrode. Due to the enhanced mass transfer, it is evident that the Li_2O_2 volume distribution of the flow model is more uniform, and the whole electrode is much better utilized than that of the static model. The same group also reported a further-improved two-dimensional and transient model, considering electrolyte concentration, oxygen concentration, electrolyte potential, electrode potential, and the porosity change caused by Li_2O_2 precipitation.[160] In this work, two more designs were tested, including a dual layer air electrode and alternating flow. The dual layer air electrode is equipped with uneven porosity for better pore utilization of the air electrode. When the oxygen side has a higher porosity (0.9) and the separator side has a lower porosity (0.7), the specific capacity is 105% higher than that with uniform porosity. Alternating flow is a design that can change the flow direction to fully utilize the micro-pores samely, and the calculated results show that the capacity is improved by 3% at a current density of 0.2 mA cm^{-2}. Apart from the

View Article Online
DOI: 10.1039/C9TA10658H

two aforementioned designs, the distribution of Li_2O_2 volume fraction (ε_{Li2O2}) at different current densities was also studied. It is found that a higher Li_2O_2 volume fraction emerged at a lower discharge current. Additionally, the Li_2O_2 fraction close to the inlet reached the maximum value due to a high reaction rate caused by a higher oxygen concentration. Previous work has demonstrated that oxygen transport is one of the most important factors that affect the battery performance. The impacts of two most important parameters for oxygen transport on static and flow LABs, including oxygen diffusion coefficient (D_{O2}) and solubility ($c_{O2;sat}$), are illustrated in Fig. 9c and 9d. At the same value of D_{O2} or $c_{O2;sat}$, the specific capacity of the flow battery is always higher than that of the static one. Even when the D_{O2} decreases to nearly zero, the specific capacity still maintains a relatively high value due to the oxygen transport, originated from convection. The air electrode thickness is also crucial to achieving the power density and energy density. Four different thicknesses (400, 600, 800, and 1000 μm) were employed in the static and flow models, respectively. In the static battery, the specific capacity becomes stable when the cathode thickness increases, while in a flow battery, the best thickness appears to get the maximum specific capacity. As pump work is an inevitable part in LAFBs for practical applications, is the work found that 0.4 atm is an optimal pressure difference when the flow design can improve the capacity to 15 times than that of the static one, and the pump work only occupies 10% of the total energy output. More recently, a novel modeling method for LAFB designs has been proposed by Poli and his co-workers.[187] This work reports a semi-empirical model which associates the net power output with the 3D cathode

View Article Online
DOI: 10.1039/C9TA10658H

geometry. Different from the aforementioned modeling works, the model is based on the experimental data without the demands of kinetics data, which dramatically diminishes the modeling complexity of LAFB.

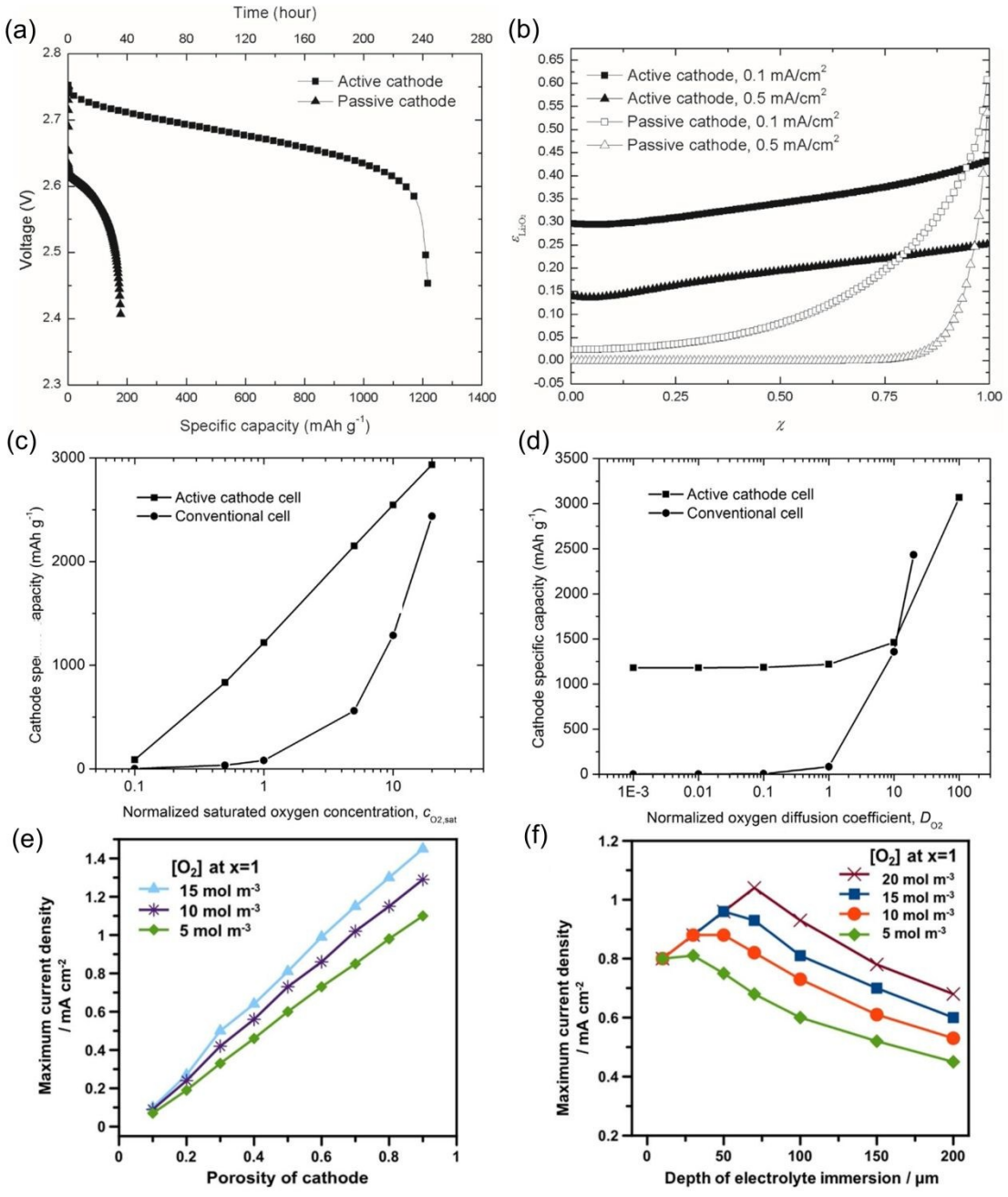

Fig. 9 (a) Comparison of voltage vs. specific capacity curves between the lithium-air cells with passive and active air electrode. The discharge current density is 0.2 mA cm^{-2}. (b) Distributions of volume fractions of Li_2O_2 in the electrode after the passive and the active lithium cells are fully

View Article Online
DOI: 10.1039/C9TA10658H

discharged at different current densities. Reproduced with permission from ref. 186. Copyright 2015, Elsevier. (c and d) The impacts of (c) the oxygen diffusion coefficient, D_{O2} and (d) the oxygen solubility, $c_{O2;sat}$ on the air electrode. Reproduced with permission from ref. 160. Copyright 2015, Elsevier. (e and f) Simulation results of maximum current density that can be achieved as a function of (e) cathode porosity, ranging from 0.1 to 0.9 and (f) depth of cathode immersion, ranging from 10 to 200 mm for different initial concentrations of O_2 (5, 10, 15 and 20 mol m^{-3}) in N,N-di-ethyl-N-(2-methoxyethyl)-N-methylammonium bis(trifluoromethylsulfonyl)i-mide (DEME–TFSI, 3300 mol m^{-3} of $DEME^+$). Reproduced with permission from ref. 105. Copyright 2017, Wiley.

To investigate the impacts of the air electrode parameters on LAFBs, a numerical investigation was carried out based on a static battery model with assumptions on the Li_2O_2 solubility to simulate the influence of flow.[105] In the flow system, the solubility of Li_2O_2 was set to be infinity (1000000 mol m^{-3}), different from that in the static case (0.09 mol m^{-3}). Focused on the optimized gas diffusion layer (GDL), the optimal values of two parameters (porosity and depth of immersion of electrode by electrolyte) were investigated. As shown in Fig. 9e the maximum current density is always proportional to the porosity at different initial oxygen concentrations because of a higher oxygen transport rate in a higher porosity. However, as shown in Fig. 9f, an optimal value exists to get the best performance for a specific oxygen concentration.

The modeling works on LAFBs are still at very early stages, and only the discharge process has been studied. As the charge process is related to the cycle life, the corresponding modeling works should be performed. Moreover, design

View Article Online
DOI: 10.1039/C9TA10658H

parameters, such as the flow field design, pump work, are required to be further investigated.

4.1.2 Experimental investigations

Experimental investigations have also been conducted to investigate the effects of flow media on LAFBs. Fig. 10a shows a schematic diagram of a LAFB, which employs an ionic liquid (IL), N,N-di-ethyl-N-(2-methoxyethyl)-N-methylammonium bis(trifluoromethylsulfonyl)i-mide (DEME–TFSI), as the flow medium; while 1 M LiTFSI dissolved in propylene carbonate used as the electrolyte for the lithium anode is static.[105] The comparison of the discharge profiles with and without electrolyte flowing at the current density of 0.077 mA cm^{-2} is shown in Fig. 10b. Apparently, the flow battery operates stably and exhibits a higher capacity than that of the static one, suggesting that the initial discharge product, superoxide anion radical O− 2, is effectively removed from the cathode surface and transported into the bulk electrolyte by the mechanical flow of the ionic liquid. However, both the static and the flow batteries show relatively low voltages, which is attributed to the large overpotentials caused by the low diffusivity of O− 2 in the IL lacking Li salts. IL-based electrolytes have been considered to be promising candidate electrolytes for LABs in recent years owing to the high stability toward superoxide, wide electrochemical stability window, low volatility, non-flammable, high safety, good conductivity, and hydrophobicity.[188–194] However, the main problem for LABs employing IL-based electrolytes is the worse performance at high discharge current densities, which is

View Article Online
DOI: 10.1039/C9TA10658H

mainly caused by the sluggish oxygen transport.[188] To investigate the effects of flow system on oxygen transport in IL-based electrolytes, a novel structure for LAFBs with an oxygen-bubbling device (OBD) was developed by Monaco, as shown in Fig. 10c.[188] One kind of O_2-saturated IL, N-butyl-N-methyl pyrrolidinium bis(trifluoromethanesulfonyl)imid ($PYR_{14}TFSI$), mixed with LiTFSI, was used as the electrolyte for the LAFB with a meso-macroporous carbon (ZL)-coated glassy carbon (ZL/GC) electrode. $PYR_{14}TFSI$ is a promising electrolyte for LAFBs due to its good compatibility with lithium metal[195,196] and relatively high oxygen solubility (2.9–3.1 mm at 25-30 ^oC) and oxygen diffusion coefficient (8.8×10^{-6} cm^2 s^{-1}).[190,197,198] The discharge/charge profiles in static and flow conditions at a current density of 0.2 mA cm^{-2} are shown in Fig. 10d. It is evident that the flowing electrolyte can dramatically ameliorate the battery performance, especially the discharge capacity. The specific capacity and coulombic efficiency are 600 mAh g^{-1} and 91.8%, respectively. Latter, a scale-up LAFB prototype with a similar structure and the same electrolyte was reported, in which a new mesoporous carbon (C250) was attempted.[198,199] The specific capacity ranges from 700–1400 mA g^{-1} at different carbon substrates and operation temperatures; while the coulombic efficiency is low, which is because of the parasitic reactions and the detachment of the discharge product caused by the flowing electrolyte during the OER.[200]

View Article Online
DOI: 10.1039/C9TA10658H

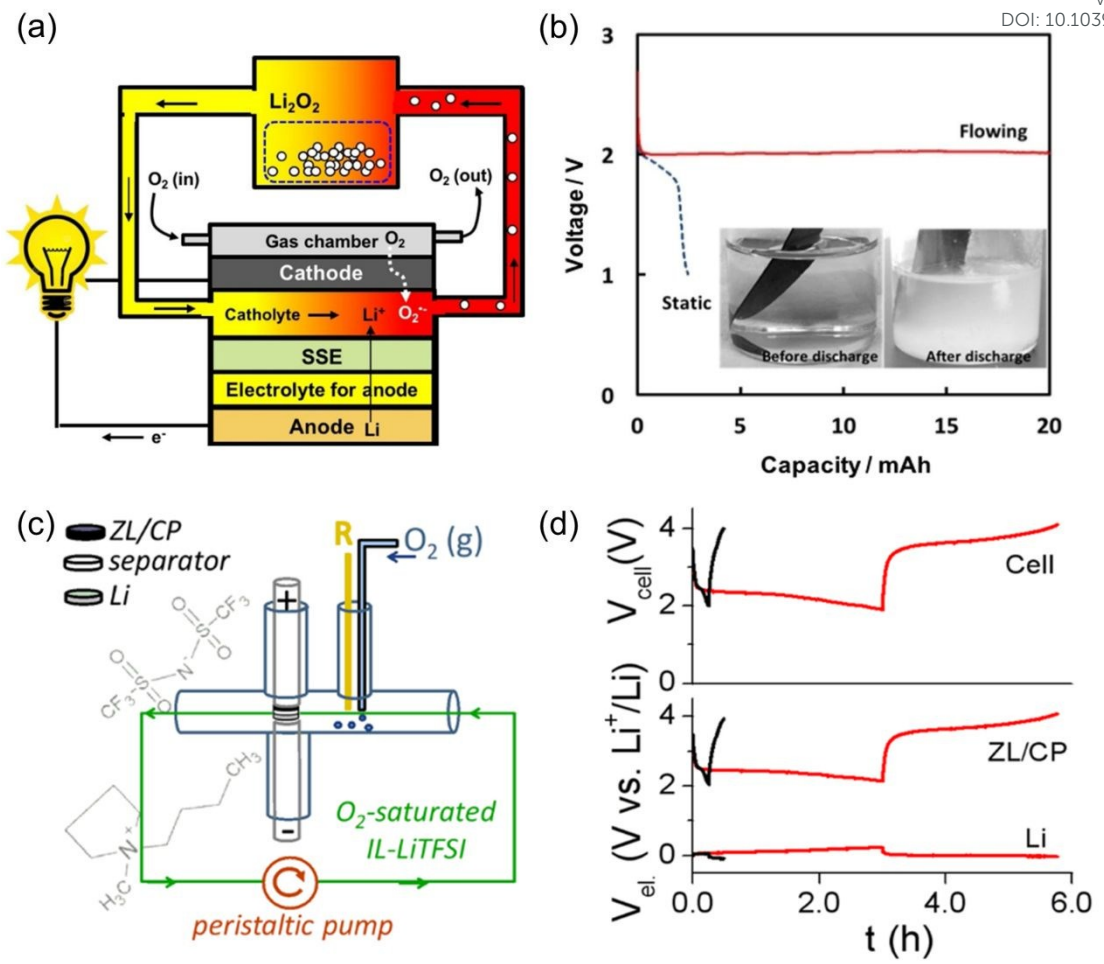

Fig. 10 (a) Schematic diagram of the LAFBs, and the electrolyte is N,N-di-ethyl-N-(2-methoxyethyl)-N-methylammonium bis(trifluoromethylsulfonyl)imide (DEME–TFSI). (b) Discharge behavior of non-aqueous LABs with and without flowing catholyte. Reproduced with permission from ref. 105. Copyright 2017, Wiley. (c) Scheme of the flow IL-based lithium-air battery (R stands for reference electrode). (d) Flow battery voltage and ZL/CP and Li electrode potentials vs Li^+/Li upon discharge/recharge cycles at room temperature and 0.2 mA cm^{-2}: 1st cycle (black curves) with the pump off and 2nd cycle (red curves) with the pump on. Reproduced with permission from ref. 188. Copyright 2013, ACS Publications.

View Article Online
DOI: 10.1039/C9TA10658H

4.2 Semi-solid flow design

To achieve high energy and power density, the concept of semi-solid, fluidic electrodes have been employed in Li/Na-ion batteries,[201] supercapacitors,[202] and LABs.[203] In SectionTwo, the metal electrode can be a semi-solid, fluidic electrode in ZAFBs, in which particles are mixed into the electrolyte to form a slurry. In LAFBs based on non-aqueous electrolytes, since the air electrode is the main component that limits the battery performance, a semi-solid catholyte was thus reported.[108] As shown in Fig. 11a and 11b, the battery employed a semi-solid catholyte composed of 2 wt% Super P (SP) carbon suspending in O_2-saturated tetraethylene glycol dimethyl ether (TEGDME)-LiTFSI. The current collector of the air electrode is a carbon percolating network composed of SP-coated Reticulated Vitreous Carbon (RVCSP). During discharge, the ORR takes place and the Li_2O_2 deposits on the SP particle surfaces. Thus, the passivation and clogging issues of the air electrode are addressed, and the discharge product can be easily electrochemically oxidized. Besides, the reaction surface is expanded due to the carbon percolating network of the semi-solid component, accelerating the reaction rate and enhancing the performance at high current densities. The semi-solid flow prototype demonstrates higher performance over conventional LABs, including a high current density up to 4 mA cm^{-2}, a high capacity of 175 mAh cm^{-2}, and a peak power density of 7.5 mW cm^{-2}, as presented in Fig. 11c. Notably, the results manifest that the performance of the battery is affected by the lithium anode rather than the cathode and catholyte, which is definitely different from conventional lithium-air flow batteries. This indicates the battery

View Article Online
DOI: 10.1039/C9TA10658H

performance can be further improved by developing a high-performance lithium electrode. On the basis of this work, the same group conducted further works on the effects of different compositions of the catholyte on battery performance.[204,205] The influence of different weight percentage of Super P (SP) from 2 wt.% to 20wt.% was firstly investigated,[204] and the results show that the specific energy and energy density of 12 wt.% SP are 10 times higher than that of 2 wt.% SP. When the weight percentage of SP is > 12%, the specific energy and energy densities are predicted to reach more than 1 kWh kg^{-1} and 1 kWh L^{-1}, respectively. Then, the electrochemical properties of other types of carbon particles, Pureblack carbon (PB), with different weight percentages (2 wt.%: PB2, 10 wt.%: PB10) were tested.[205] At the current density of 0.25 mA cm^{-2}, the use of high weight percentage of PB (PB10) decreases the overpotential of the cathode effectively, in which the V_{cath} of SP2, PB2, and PB10 are 2.32, 2.47 and 2.74 V vs. Li/Li^+, respectively. Moreover, viscosity has a great impact on the flow of the electrolyte. As shown in Fig. 11d, 10PB and 2SP catholytes have the same viscosity curves basically while the former has better electrochemical performance. More importantly, the high concentrated PB demonstrates pseudoplastic behaviors. Thus, it is possible to decouple the lower pump energy consumption and higher energy output of the semi-solid LAFB by employing reasonably concentrated carbon particles and appropriate flow field designs.

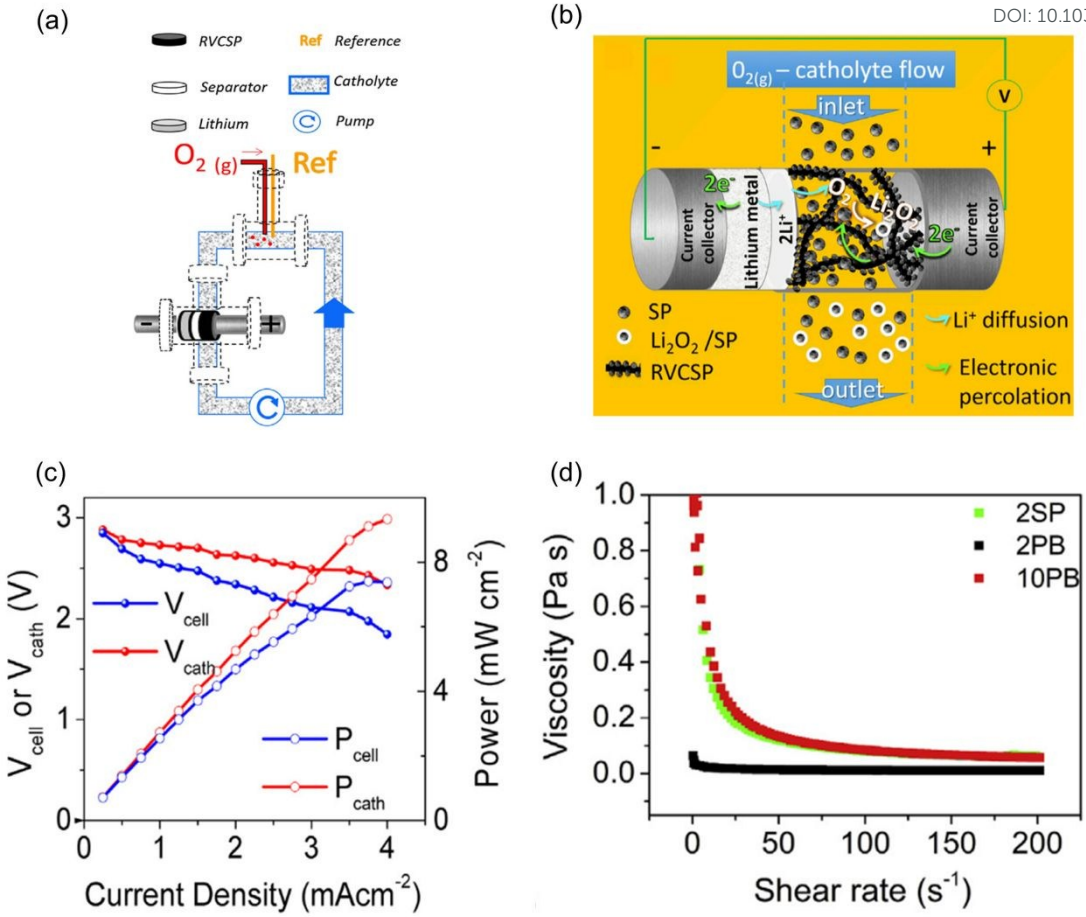

Fig. 11 The semi-solid lithium-air flow battery scheme (a) and (b) and the prototype under operation. (c) cell and cathode discharge polarization curves and power vs. current plots. Reproduced with permission from ref. 106. Copyright 2018, Elsevier. (d) Viscosity (η) vs. shear rate (γ) of the 2SP, 2 PB and 10 PB catholytes. Reproduced with permission from ref. 205. Copyright 2018, Elsevier.

4.3 Functional additives

To further address surface passivation and pore clog of the air electrode caused by the insoluble Li_2O_2, soluble redox mediators (RMs), originated from the concept of ‘‘redox targeting’’ reactions proposed for LIBs[206–208] and static LABs,[93,209,210] have been introduced to LAFBs. A LAFB with soluble RMs in aqueous catholyte was

View Article Online
DOI: 10.1039/C9TA10658H

firstly proposed by Wang and his co-workers.[211] Latter, Zhu et al. conducted several experimental works employing redox mediators.[212–214] As shown in Fig. 12a,[212] during discharge, redox mediator RM_1 is firstly reduced on the air electrode:

$$RM_1^{OX} + e^- \longrightarrow RM_1^{red} \quad (10)$$

and then the reduced product reacts with Li^+-ions in the tank:

$$2Li^+ + 2RM_1^{red} + O_2 \longrightarrow Li_2O_2 + 2RM_1^{OX} \quad (11)$$

In this process, RM_1 regenerates and Li_2O_2 precipitates in the tank, avoiding the pore clog issue. During charge, another soluble mediator RM_2 is oxidized on the air electrode:

$$RM_2^{red} \longrightarrow RM_2^{OX} + e^- \quad (12)$$

and the product flows into the tank and oxidizes solid Li_2O_2:

$$Li_2O_2 + 2RM_2^{OX} \longrightarrow 2Li^+ + 2RM_2^{red} + O_2 \quad (13)$$

Evidently, RM_1 and RM_2 play important roles in the discharge and charge processes. Zhu et al. selected ethyl viologen (EV) and iodide as redox catalysts due to their redox potentials, shown in Fig. 12b.[212] Fig. 12c manifests the discharge/charge curves and the coulombic efficiency of the LAFB incorporated with RMs. No deterioration of the charge capacity was observed in the first 30 cycles. Instead, due to improved conductivity of the composite membrane used to protect the lithium electrode, the charge capacity was even enhanced with the coulombic efficiency of nearly 100% after the 10th cycle. Later, the same group developed another two soluble catalysts, 2,5-di-*tert*-butyl-*p*-benzoquinone (DTBBQ) and tris{4-[2-(2-methoxyethoxy)ethoxy]phenyl}amine (TMPPA), for the ORR and OER

View Article Online
DOI: 10.1039/C9TA10658H

processes, respectively, as shown in Fig. 12d. The battery with these two soluble catalysts demonstrated high stability in 100 cycles.[213] More recently, a LAFB with a spraying nozzle and an electrolyte collection tank was reported to further improve reaction kinetics of the ORR (Fig. 12e).[214] The nozzle increased the reaction areas and thus accelerated the ORR rate. In this battery, a new redox soluble catalyst, duroquinone (DQ), which has superior electrochemical reversibility and a higher diffusion coefficient than another two RMs (EV, DTBBQ), was introduced to the EV-based electrolyte to form EV-DQ dual RM electrolyte. Fig. 12f shows the voltage profiles of the battery operating in pure oxygen and dry air with the EV-DQ (0.2 M / 0.2M) dual RM electrolyte. In the pure oxygen condition, the battery achieved a peak power density of 60 mW cm^{-2}. In addition, the utilization of lithium metal loaded in the negative electrode reached 80% at a constant current density of 15 mA cm^{-2}. When the current density decreased to 1 mA cm^{-2}, the utilization further increased to above 90%. When the battery was in the dry air condition, it operated steadily at a power density of about 22 mW cm^{-2} and the peak power density reaches 34 mW cm^{-2} with the lithium utilization of around 90%. To test the cycling stability of the battery and the robustness of the ORR process, a device to mechanically refuel the lithium metal is designed instead of introducing an OER redox catalyst. By refueling fresh Li foil, the battery operated stably at 10 mA cm^{-2} with a capacity of around 140 mA h cm^{-2} in the first two feeds.

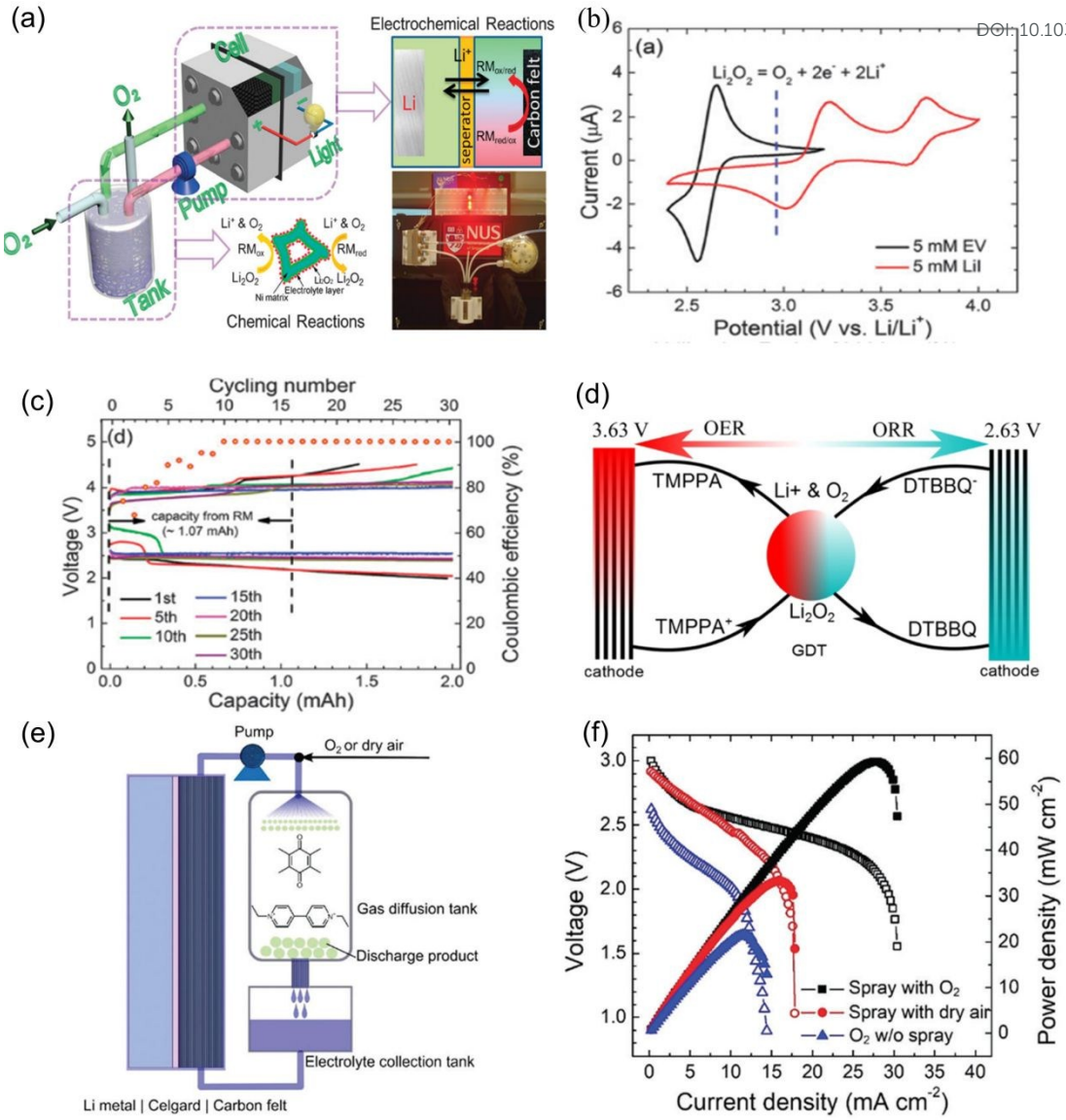

Fig. 12 (a) Schematic illustration of the configuration and working process of a redox flow lithium-oxygen battery (RFLOB). The cell stack constitutes a lithium metal anode and a carbon felt cathode (2 cm x 2cm), separated by a membrane. A gas diffusion tank (GDT) is connected to the cathodic compartment through a pump. During the discharging process, oxygen flows into the tank and is reduced to form Li_2O_2 while the electrolyte fluid containing redox mediators and Li^+ circulates between GDT and the cell. The photo at the lower right corner shows an RFLOB single cell powering three light-emitting diodes. (b) Cyclic voltammograms of EV and LiI in TEGDME. The scan rate is 0.10 V s^{-1}. The redox potential of Li_2O_2 is indicated for reference. (c)

View Article Online
DOI: 10.1039/C9TA10658H

Discharge/charge curves and Coulombic efficiency of an RFLOB employing a PVDF–Nafion membrane at different cycle numbers. The current density is 0.125 mA cm^{-2}. Reproduced with permission from ref. 212. Copyright 2015, The Royal Society of Chemistry. (d) Diagram describing DTBBQ- and TMPPA-catalyzed ORR and OER reactions during the charging and discharging processes of RFLOB. Reproduced with permission from ref. 213. Copyright 2016, ACS Publications. (e) Configuration of an RFLOB cell system (single cell) with integrated electrolyte spray. (f) Voltage and power density vs. current density curves of RFLOB cells under different operating conditions. The electrolyte was EV-DQ (0.2 M/0.2 M) in 1 M LiTFSI/DSMO. Reproduced with permission from ref. 218. Copyright 2017, The Royal Society of Chemistry.

The introduction of redox mediators to LAFBs is a promising way to address the problems caused by solid products and by-products, which combines the advantages of redox mediators and unique flow structures, but the stability of redox mediators and the corresponding structure designs for effective operation still need further investigations.

4.4 Summary of non-aqueous metal-air flow batteries

Table 2 Summary of non-aqueous metal-air flow batteries

Metal electrode	Air electrode	Electrolyte	Atmosphere	Electrochemical performance	Ref
Lithium metal	ZL/GC	Pyr_{14}TFSI-LiTFSI	Oxygen	Specific capacity: 600 mAh g^{-1} Coulombic efficiency: 91.8%	[188]
Lithium metal	ZL or C250	Pyr_{14}TFSI-LiTFSI	Oxygen	Specific capacity: 1445 mAh g^{-1} Coulombic efficiency: 49%	[198]

Lithium metal	Micro-porous layer	DEME–TFSI	Oxygen		[105]
Lithium metal	Carbon paper	TEGDME-LiTFSI-Super P	oxygen	Discharge capacity: >175 mAh cm^{-2} Energy desntiy: > 500 mWh cm^{-2} Power density: > 7 mW cm^{-2}	[108]
Lithium metal	Carbon felt	TEGDME-LiTFSI-EV-I_2	oxygen	Coulombic efficiency: 100% Cyclability:>30 cycles at 0.125 mA cm^{-2}	[212]
Lithium metal		TEGDME-LiTFSI-DTBBQ-TMPPA	oxygen	Cyclability: >100 cycles at 0.5 mA cm^{-2}	[213]
Lithium foil	Carbon felt	DSMO-LiTFSI-EV-DQ	Dry air	Power density: 34 mW cm^{-2} Areal capacity: 140 mA h cm^{-2} at 10 mA cm^{-2}	[214]

From Table 2, the reported works of non-aqueous LAFBs mainly focus on developing novel structures (e.g., semi-solid air electrode design) and employing new materials (e.g., IL-based electrolytes, redox mediators) with the assistance of flow field to address the intrinsic problems. Obviously, the battery performance is effectively improved by employing those novel structures and materials, but many problems still exist. First, the power densities are still far lower than those of ZAFBs, which is caused by the low operating current densities of LAFBs. Second, most of the used gas is still pure oxygen, and the performance suffers from a sharp decrease when replacing pure oxygen by dry air, which is impractical for future applications. Third, the cycling stability is still insufficient even compared with static LABs. These problems are still needed to be addressed in future works.

View Article Online
DOI: 10.1039/C9TA10658H

5. Conclusions and perspectives

In conclusion, MAFBs have many advantages over other energy storage systems due to the high capacity, remarkable energy density, and low cost. Crucial works and developments of MAFBs have been done in the past decades, most of which focus on aqueous ZAFBs and non-aqueous LAFBs. For ZAFBs, the enhancements of flow media on battery performance have been investigated. Simultaneously, several designs and additives have been reported to improve the zinc electrodes, and plenty of structures and catalysts have been applied to fabricate effective air electrodes. With respect to LAFBs, novel concepts combining with flowing media have been proposed to address the intrinsic problems. Although promising steps toward practical applications have been achieved, the remaining challenges, such as low energy efficiency of ZAFBs, low power density of LAFBs, and insufficient cycle life of both, should be addressed.

For ZAFBs, (i) the effects of different flow fields on the triple-phase boundaries need to be further investigated. In ZABs, the triple-phase boundaries in the air electrode play key roles in the ORR. The introduction of flowing media, on the one hand, may change the morphology of the solution and gas phases, and thus influences the reaction process. Apparently, different flow fields and rates have different effects on the reaction interfaces. On the other hand, during the long-term operation, the flowing media will exert an additional pressure difference on the air electrode, which may damage the microporous structure and deteriorate the hydrophobicity of the gas diffusion layer. However, few efforts have been made to give an insight view of these

View Article Online
DOI: 10.1039/C9TA10658H

impacts. (ii) morphological changes of the electrodes caused by flow media should be considered. Although it is revealed that the flow media can suppress dendrite effectively, while the electrodes may suffer from shape changes in the flow field. For zinc electrodes, the zinc atoms close to the inlet will be transferred to other parts for deposition during charge, which consequently results in shape changes of the zinc electrode. In some reported zinc-based batteries, a porous zinc electrode is employed to increase the reaction area.[129] Although dendrites of zinc plates can be effectively addressed by flow media, the impacts of flow media on dendrites and shape changes of porous zinc electrodes are still unclear. For air electrodes, the morphology and porous structures may also be changed under the influence of flow media. Thus, the novel electrode and flow field designs are important to alleviate or eliminate the negative effects. (iii) the effects of flow media on the charge process and cycling stability need to be investigated. For secondary ZABs, due to the resistance of the gas diffusion layer, gaseous oxygen accumulation during charge is a severe problem that limits the performance. The generated oxygen bubbles will accumulate on the surface of the air electrode and thus reduce the reaction areas. More importantly, the bubbles increase the inner pressure of the battery, causing the leakage of electrolyte and the degradation of hydrophobicity, decreasing the cycle life. Although introducing flowing electrolyte has been proven to improve the charge performance, while the intrinsic mechanisms, especially from the oxygen transport perspectives, should be further illustrated.

For LAFBs, (i) modeling works need to be further conducted to reveal the effects

View Article Online
DOI: 10.1039/C9TA10658H

of flow media on oxygen transport. In most reported works, dissolved oxygen in the electrolyte is taken as the reactant in simulation. However, this is not a practical situation for battery operation due to an additional oxygen dissolution process. (ii) novel reaction interface designs are needed. To improve the power density, artificial triple-phase boundaries by developing an electrolyte comprising of two immiscible components has been reported, in which one component has an excellent oxygen transport ability while the other is a non-aqueous polar liquid with high Li^+ transport ability.[215] This probably is a good concept for the development of flow media that can further accelerate oxygen transport and reaction rates. (iii) the cyclability is demanded to be further improved. The passivation of lithium metal, limited reaction interfaces of solid products, and parasitic reactions make the battery have poor reversibility. For most experimental and modeling works, the electrical charge process and cyclability are rarely considered, which may be significantly different when the flowing electrolyte is introduced. (iv) designs of the flow path and the storage tank are demanded for solving the pore clog problem. During discharge, the flow media bring the generated solid product out of the battery and the products are stored in the tank, which will return to the air electrode to be decomposed during charge. On the one hand, a corresponding structure used for avoiding the clog in the flow path and the storage tank is important for long-term operation. On the other hand, for the electrolyte is circulating constantly during operation, it is essential to allow the solid product to remain in the tank during discharge and react thoroughly in the air electrode during charge.

View Article Online
DOI: 10.1039/C9TA10658H

The designs of MAFB stack are important for practical applications. When the battery size is scale-up, the battery performance may decrease dramatically.[101,122] In addition, as a half-open system, the electrolyte leakage becomes pretty severe. Therefore, developing stacks comprising of small battery units is a promising way. Due to the demands of ambient air and flow electrolyte, the mass transfer in the stack is a key point. First, an appropriate stack design is needed to meet the consumption of air. Second, a storage tank is commonly placed outside the battery to store the electrolyte. As it is impossible that every single battery has an independent storage tank, one or several storage tanks of a stack as the container of electrolyte and manifolds are applied to distribute the electrolyte. For the electrolyte with high conductivity in the manifolds, a new problem of shunt currents appears, which greatly reduces coulombic efficiency and causes energy loss.[144] Although many works about shunt currents in RFBs have been reported in recent years,[216–220] reasonable flow channel and battery structure designs are crucial.

In most reported works, the battery performance increment originated from the flow system is only considered. However, the negative impacts are also obvious. First, the external storage tank and flow pipes occupy a large space, which not only makes the battery structure complicated but also decrease the practical specific capacity. Usually, the volume of the storage tank unit is larger than that of the battery unit, and hence the specific capacity of the whole battery is greatly reduced for which the MAFBs may lose the most important advantages of high capacity for portable electronics and electric vehicles. Second, pump work is an inevitable part of the

View Article Online
DOI: 10.1039/C9TA10658H

whole battery system, and only few modeling works considered the pump work by pure theoretical calculations,[160,186] which is not very accurate due to the assumptions in viscosity, temperature, and flow channel structure. In section 4.1.1, we have introduced a semi-emprical model for calculating the net power output of LAFBs,[187] while further works are still needed to balance the pump work and output power in practical applications.

At last, the working conditions need to be considered comprehensively. First, due to the semi-open structure, the evaporation of the electrolyte, which may be accelerated by the flow media, is inevitable and irreversible. Although the storage tank can store plenty of electrolytes, the evaporation problem cannot be ignored in the long-term operation. In addition, Parasitic reactions caused by carbon dioxide and moisture contaminations from the ambient air deteriorate the battery performance. For ZAFBs, carbonates will form in the presence of CO_2, which reduce the surface area of the porous electrode and deteriorate the conductivity of the alkaline electrolyte.[81] For LAFBs, when the non-aqueous electrolyte is mixed with moisture, the lithium electrode will be corroded and the overpotential will also increase.[221] More importantly, both moisture and CO_2 can participate in the electrochemical reactions on the surface of the air electrode and lead to poor cycle life.[222] Further, the operating temperatures, either hot or cold, can change the performance. Thus, the detailed influences should be revealed, and proper management methods should be developed.

In summary, MAFBs are promising next-generation energy storage systems with wide potential applications. Although the development of MAFBs is still in its

View Article Online
DOI: 10.1039/C9TA10658H

infancy, the experimental and theoretical efforts, together with the developments of materials and structure, as well as characterization methods, will surely accelerate the commercialization.

Declaration of interests

The authors declare no competing interests.

Acknowledgments

P. Tan thanks the funding support from CAS Pioneer Hundred Talents Program and USTC Tang Scholar. Z. Wu thanks the funding support from Hong Kong Scholar Program (XJ2017023) and the National Natural Science Foundation of China (21736008). M. Ni thanks the funding support from The Hong Kong Polytechnic University (G-YW2D) and a grant (Project Number: PolyU 152214/17E) from Research Grant Council, University Grants Committee, Hong Kong SAR.

Reference

1 C. Breyer and A. Gerlach, *Prog. photovoltaics Res. Appl.*, 2013, **21**, 121–136.

2 Q. Jiang, M. Z. Qu, G. M. Zhou, B. L. Zhang and Z. L. Yu, *Mater. Lett.*, 2002, **57**, 988–991.

3 V. Paladini, T. Donateo, A. de Risi and D. Laforgia, *Energy Convers. Manag.*, 2007, **48**, 3001–3008.

View Article Online
DOI: 10.1039/C9TA10658H

4 M. Zhi, C. Xiang, J. Li, M. Li and N. Wu, *Nanoscale*, 2013, **5**, 72–88.

5 Y. Zhu, S. Murali, M. D. Stoller, K. J. Ganesh, W. Cai, P. J. Ferreira, A. Pirkle, R. M. Wallace, K. A. Cychosz, M. Thommes, D. Su, E. A. Stach and R. S. Ruoff, *Science*, 2011, **332**, 1537–1541.

6 W. K. Chee, H. N. Lim, Z. Zainal, N. M. Huang, I. Harrison and Y. Andou, *J. Phys. Chem. C*, 2016, **120**, 4153–4172.

7 M. Vangari, T. Pryor and L. Jiang, *J. Energy Eng.*, 2012, **139**, 72–79.

8 P. Denholm and R. Sioshansi, *Energy Policy*, 2009, **37**, 3149–3158.

9 H. L. Ferreira, R. Garde, G. Fulli, W. Kling and J. P. Lopes, *Energy*, 2013, **53**, 288–298.

10 E. Drury, P. Denholm and R. Sioshansi, *Energy*, 2011, **36**, 4959–4973.

11 M. Budt, D. Wolf, R. Span and J. Yan, *Appl. Energy*, 2016, **170**, 250–268.

12 K. Pielichowska and K. Pielichowski, *Prog. Mater. Sci.*, 2014, **65**, 67–123.

13 A. Sharma, V. V. Tyagi, C. R. Chen and D. Buddhi, *Renew. Sustain. Energy Rev.*, 2009, **13**, 318–345.

14 G. G. D. Han, H. Li and J. C. Grossman, *Nat. Commun.*, 2017, **8**, 1446.

15 J. P. Deane, B. P. Ó Gallachóir and E. J. McKeogh, *Renew. Sustain. Energy Rev.*, 2010, **14**, 1293–1302.

16 D. Connolly, H. Lund, P. Finn, B. V. Mathiesen and M. Leahy, *Energy Policy*, 2011, **39**, 4189–4196.

17 C. J. Yang and R. B. Jackson, *Renew. Sustain. Energy Rev.*, 2011, **15**, 839–844.

18 B. Dunn, H. Kamath and J. M. Tarascon, *Science*, 2011, **334**, 928–935.

View Article Online
DOI: 10.1039/C9TA10658H

19 V. Etacheri, R. Marom, R. Elazari, G. Salitra and D. Aurbach, *Energy Environ. Sci.*, 2011, **4**, 3243–3262.

20 L. Lu, X. Han, J. Li, J. Hua and M. Ouyang, *J. Power Sources*, 2013, **226**, 272–288.

21 G. Zubi, R. Dufo-López, M. Carvalho and G. Pasaoglu, *Renew. Sustain. Energy Rev.*, 2018, **89**, 292–308.

22 J. Zhu, T. Wierzbicki and W. Li, *J. Power Sources*, 2018, **378**, 153–168.

23 K. Liu, Y. Liu, D. Lin, A. Pei and Y. Cui, *Sci. Adv.*, 2018, **4**, eaas9820.

24 X. Feng, M. Ouyang, X. Liu, L. Lu, Y. Xia and X. He, *Energy Storage Mater.*, 2018, **10**, 246–267.

25 R. Schmuch, R. Wagner, G. Hörpel, T. Placke and M. Winter, *Nat. Energy*, 2018, **3**, 267–278.

26 M. Xu, D. G. Ivey, Z. Xie and W. Qu, *J. Power Sources*, 2015, **283**, 358–371.

27 H. Geaney, J. O'Connell, J. D. Holmes and C. O'Dwyer, *J. Electrochem. Soc.*, 2014, **161**, A1964–A1968.

28 R. Cao, E. D. Walter, W. Xu, E. N. Nasybulin, P. Bhattacharya, M. E. Bowden, M. H. Engelhard and J. G. Zhang, *ChemSusChem*, 2014, **7**, 2436–2440.

29 W. G. Hardin, D. A. Slanac, X. Wang, S. Dai, K. P. Johnston and K. J. Stevenson, *J. Phys. Chem. Lett.*, 2013, **4**, 1254–1259.

30 V. Caramia and B. Bozzini, *Mater. Renew. Sustain. Energy*, 2014, **3**, 28.

31 M. A. Rahman, X. Wang and C. Wen, *J. Appl. Electrochem.*, 2014, **44**, 5–22.

32 J. Zhang, W. Xu and W. Liu, *J. Power Sources*, 2010, **195**, 7438–7444.

View Article Online
DOI: 10.1039/C9TA10658H

33 T. Kuboki, T. Okuyama, T. Ohsaki and N. Takami, *J. Power Sources*, 2005, **146**, 766–769.

34 M. Balaish, A. Kraytsberg and Y. Ein-Eli, *Phys. Chem. Chem. Phys.*, 2014, **16**, 2801–2822.

35 M. K. Song, S. Park, F. M. Alamgir, J. Cho and M. Liu, *Mater. Sci. Eng. R Reports*, 2011, **72**, 203–252.

36 J. Wang, Y. Li and X. Sun, *Nano Energy*, 2013, **2**, 443–467.

37 M. Prabu, K. Ketpang and S. Shanmugam, *Nanoscale*, 2014, **6**, 3173–3181.

38 R. D. McKerracher, C. Alegre, V. Baglio, A. S. Aricò, C. Ponce De León, F. Mornaghini, M. Rodlert and F. C. Walsh, *Electrochim. Acta*, 2015, **174**, 508–515.

39 A. Vignesh, M. Prabu and S. Shanmugam, *ACS Appl. Mater. Interfaces*, 2016, **8**, 6019–6031.

40 J. Lu, Y. Lei, K. C. Lau, X. Luo, P. Du, J. Wen, R. S. Assary, U. Das, D. J. Miller, J. W. Elam, H. M. Albishri, D. A. El-Hady, Y. K. Sun, L. A. Curtiss and K. Amine, *Nat. Commun.*, 2013, **4**, 2383.

41 P. Tan, B. Chen, H. Xu, W. Cai, W. He, H. Zhang, M. Liu, Z. Shao and M. Ni, *ACS Appl. Mater. Interfaces*, 2018, **10**, 36873–36881.

42 C. C. Chang, Y. C. Lee, H. J. Liao, Y. T. Kao, J. Y. An and D. Y. Wang, *ACS Sustain. Chem. Eng.*, 2019, **7**, 2860–2866.

43 P. Tan, B. Chen, H. Xu, W. Cai, W. He, M. Liu, Z. Shao and M. Ni, *Small*, 2018, **14**, 1800225.

44 B. Li, J. Quan, A. Loh, J. Chai, Y. Chen, C. Tan, X. Ge, T. S. A. Hor, Z. Liu, H. Zhang and Y. Zong, *Nano Lett.*, 2017, **17**, 156–163.

45 W. Shang, W. Yu, P. Tan, B. Chen, H. Xu and M. Ni, *J. Power Sources*, 2019, **421**, 6–13.

46 P. Tan, B. Chen, H. Xu, W. Cai, W. He and M. Ni, *Appl. Catal. B Environ.*, 2019, **241**, 104–112.

47 P. Tan, B. Chen, H. Xu, W. Cai, M. Liu, Z. Shao and M. Ni, *J. Electrochem. Soc.*, 2018, **165**, A2119–A2126.

48 D. U. Lee, J. Fu, M. G. Park, H. Liu, A. Ghorbani Kashkooli and Z. Chen, *Nano Lett.*, 2016, **16**, 1794–1802.

49 M. Yu, X. Ren, L. Ma and Y. Wu, *Nat. Commun.*, 2014, **5**, 5111.

50 J. Lv, S. C. Abbas, Y. Huang, Q. Liu, M. Wu, Y. Wang and L. Dai, *Nano Energy*, 2018, **43**, 130–137.

51 W. Wang, Q. Luo, B. Li, X. Wei, L. Li and Z. Yang, *Adv. Funct. Mater.*, 2013, **23**, 970–986.

52 P. Alotto, M. Guarnieri and F. Moro, *Renew. Sustain. Energy Rev.*, 2014, **29**, 325–335.

53 P. Leung, X. Li, C. Ponce De León, L. Berlouis, C. T. J. Low and F. C. Walsh, *RSC Adv.*, 2012, **2**, 10125–10156.

54 A. Z. Weber, M. M. Mench, J. P. Meyers, P. N. Ross, J. T. Gostick and Q. Liu, *J. Appl. Electrochem.*, 2011, **41**, 1137–1164.

55 L. H. Thaller, US Patent 3996064, 1976.

View Article Online
DOI: 10.1039/C9TA10658H

56 X. Zhou, L. Lin, Y. Lv, X. Zhang and Q. Wu, *J. Power Sources*, 2018, **404**, 89–95.

57 C. Ponce de León, A. Frías-Ferrer, J. González-García, D. A. Szánto and F. C. Walsh, *J. Power Sources*, 2006, **160**, 716–732.

58 M. Skyllas-Kazacos, M. H. Chakrabarti, S. A. Hajimolana, F. S. Mjalli and M. Saleem, *J. Electrochem. Soc.*, 2011, **158**, R55–R79.

59 B. Dawoud, E. Amer and D. Gross, *Int. J. energy Res.*, 2007, **34**, 182–189.

60 C. Menictas and M. Skyllas-Kazacos, *J. Appl. Electrochem.*, 2011, **41**, 1223–1232.

61 P. Zhao, H. Zhang, H. Zhou, J. Chen, S. Gao and B. Yi, *J. Power Sources*, 2006, **162**, 1416–1420.

62 B. Dawoud, E. Amer and D. Gross, *Int. J. energy Res.*, 2012, **36**, 1105–1120.

63 Q. Wu, X. Zhang, Y. Lv, L. Lin, Y. Liu and X. Zhou, *J. Mater. Chem. A*, 2018, **6**, 20347–20355.

64 Q. Wu, Y. Lv, L. Lin, X. Zhang, Y. Liu and X. Zhou, *J. Power Sources*, 2019, **410–411**, 152–161.

65 Y. Zeng, F. Li, F. Lu, X. Zhou, Y. Yuan, X. Cao and B. Xiang, *Appl. Energy*, 2019, **238**, 435–441.

66 M. Skyllas-Kazacos, M. Kazacos and M. Cheng, *J. Appl. Electrochem.*, 1990, **20**, 463–467.

67 F. Rahman and M. Skyllas-Kazacos, *J. Power Sources*, 1998, **72**, 105–110.

68 F. Rahman and M. Skyllas-Kazacos, *J. Power Sources*, 2009, **189**, 1212–1219.

View Article Online
DOI: 10.1039/C9TA10658H

69 J. Xi, Z. Wu, X. Qiu and L. Chen, *J. Power Sources*, 2007, **166**, 531–536.

70 X. Li, H. Zhang, Z. Mai, H. Zhang and I. Vankelecom, *Energy Environ. Sci.*, 2011, **4**, 1147–1160.

71 H. Prifti, A. Parasuraman, S. Winardi, T. M. Lim and M. Skyllas-Kazacos, *Membranes (Basel).*, 2012, **2**, 275–306.

72 T. Janoschka, N. Martin, U. Martin, C. Friebe, S. Morgenstern, H. Hiller, M. D. Hager and U. S. Schubert, *Nature*, 2015, **527**, 78.

73 T. Luo, O. David, Y. Gendel and M. Wessling, *J. Power Sources*, 2016, **312**, 45–54.

74 Y. Li and H. Dai, *Chem. Soc. Rev.*, 2014, **43**, 5257–5275.

75 P. Tan, H. R. Jiang, X. B. Zhu, L. An, C. Y. Jung, M. C. Wu, L. Shi, W. Shyy and T. S. Zhao, *Appl. Energy*, 2017, **204**, 780–806.

76 P. Tan, Z. H. Wei, W. Shyy, T. S. Zhao and X. B. Zhu, *Energy Environ. Sci.*, 2016, **9**, 1783–1793.

77 X. B. Zhu, T. S. Zhao, Z. H. Wei, P. Tan and G. Zhao, *Energy Environ. Sci.*, 2015, **8**, 2782–2790.

78 S. Li, C. Cheng, X. Zhao, J. Schmidt and A. Thomas, *Angew. Chemie Int. Ed.*, 2018, **57**, 1856–1862.

79 O. Müller, S., Holzer, F., & Haas, *J. Appl. Electrochem.*, 1998, **28**, 895–898.

80 J. Fu, Z. P. Cano, M. G. Park, A. Yu, M. Fowler and Z. Chen, *Adv. Mater.*, 2017, **29**, 1604685.

81 P. Tan, B. Chen, H. Xu, H. Zhang, W. Cai, M. Ni, M. Liu and Z. Shao, *Energy*

View Article Online
DOI: 10.1039/C9TA10658H

Environ. Sci., 2017, **10**, 2056–2080.

82 M. Park, J. Ryu, W. Wang and J. Cho, *Nat. Rev. Mater.*, 2016, **2**, 16080.

83 X. Han, X. Li, J. White, C. Zhong, Y. Deng, W. Hu and T. Ma, *Adv. Energy Mater.*, 2018, **8**, 1801396.

84 J. Lee, S. T. Kim, R. Cao, N. S. Choi, M. Liu, K. T. Lee and J. Cho, *Adv. Energy Mater.*, 2011, **1**, 34–50.

85 A. Rahman, X. Wang and C. Wen, *J. ofThe Electrochem. Soc.*, 2013, **160**, A1759–A1771.

86 S. M. Hwang, W. Go, H. Yu and Y. Kim, *J. Mater. Chem. A*, 2017, **5**, 11592–11600.

87 P. He, Y. Wang and H. Zhou, *Electrochem. commun.*, 2010, **12**, 1686–1689.

88 X. J. Chen, A. Shellikeri, Q. Wu, J. P. Zheng, M. Hendrickson and E. J. Plichta, *J. Electrochem. Soc.*, 2013, **160**, A1619–A1623.

89 S. I. Smedley and X. G. Zhang, *J. Power Sources*, 2007, **165**, 897–904.

90 C. F. Zinola, A. J. Arvia, G. L. Estiu and E. A. Castro, *J. Phys. Chem.*, 1994, **98**, 7566–7576.

91 J. S. Spendelow and A. Wieckowski, *Phys. Chem. Chem. Phys.*, 2007, **9**, 2654–2675.

92 Z. L. Wang, D. Xu, J. J. Xu and X. B. Zhang, *Chem. Soc. Rev.*, 2014, **43**, 7746–7786.

93 H. D. Lim, H. Song, J. Kim, H. Gwon, Y. Bae, K. Y. Park, J. Hong, H. Kim, T. Kim, Y. H. Kim, X. Leprõ, R. Ovalle-Robles, R. H. Baughman and K. Kang,

View Article Online
DOI: 10.1039/C9TA10658H

Angew. Chemie Int. Ed., 2014, **126**, 4007–4012.

94 C. Y. Jung, T. H. Kim, W. J. Kim and S. C. Yi, *Energy*, 2016, **102**, 694–704.

95 A. R. Mainar, O. Leonet, M. Bengoechea, I. Boyano, I. De Meatza, A. Kvasha, A. Guerfi and J. A. Blázquez, *Int. J. energy Res.*, 2016, **40**, 1032–1049.

96 H. Yang, Y. Cao, X. Ai and L. Xiao, *J. Power Sources*, 2004, **128**, 97–101.

97 P. Pei, K. Wang and Z. Ma, *Appl. Energy*, 2014, **128**, 315–324.

98 S. Hosseini and S. Kheawhom, *ECS Trans.*, 2018, **85**, 15–23.

99 Y. H. Wen, J. Cheng, S. Q. Ning and Y. S. Yang, *J. Power Sources*, 2009, **188**, 301–307.

100 L. F. Arenas, A. Loh, D. P. Trudgeon, X. Li, C. Ponce de León and F. C. Walsh, *Renew. Sustain. Energy Rev.*, 2018, **90**, 992–1016.

101 B. Pichler, K. Mayer and V. Hacker, *Batter. Supercaps*, 2018, **1**, 1–10.

102 P. Pei, Z. Ma, K. Wang, X. Wang, M. Song and H. Xu, *J. Power Sources*, 2014, **249**, 13–20.

103 C. Jiratchayamaethasakul, N. Srijaroenpramong, T. Bunyangyuen, W. Arpavate, N. Wongyao, A. Therdthianwong and S. Therdthianwong, *J. Appl. Electrochem.*, 2014, **44**, 1205–1218.

104 X. W. Keliang Wang, Pucheng Pei, Ze Ma, Huachi Xu, Pengcheng Li, *J. Power Sources*, 2014, **271**, 65–75.

105 B. Kim, K. Takechi, S. Ma, S. Verma, S. Fu, A. Desai, A. S. Pawate, F. Mizuno and P. J. A. Kenis, *ChemSusChem*, 2017, **10**, 4198–4206.

106 R. S. Assary, J. Lu, P. Du, X. Luo, X. Zhang, Y. Ren, L. A. Curtiss and K.

View Article Online
DOI: 10.1039/C9TA10658H

Amine, *ChemSusChem*, 2013, **6**, 51–55.

107 D. Geng, N. Ding, T. S. A. Hor, S. W. Chien, Z. Liu, D. Wuu, X. Sun and Y. Zong, *Adv. Energy Mater.*, 2016, **6**, 1502164.

108 I. Ruggeri, C. Arbizzani and F. Soavi, *Electrochim. Acta*, 2016, **206**, 291–300.

109 S. S. Zhang, D. Foster and J. Read, *J. Power Sources*, 2010, **195**, 1235–1240.

110 H. Kitaura and H. Zhou, *Adv. Energy Mater.*, 2012, **2**, 889–894.

111 J. Kumar and B. Kumar, *J. Power Sources*, 2009, **194**, 1113–1119.

112 B. J. Hopkins, Y. Shao-horn and D. P. Hart, *Science*, 2018, **362**, 658–661.

113 T. Zhang, Z. Tao and J. Chen, *Mater. Horizons*, 2014, **1**, 196–206.

114 S. Yang and H. Knickle, *J. Power Sources*, 2002, **112**, 162–173.

115 M. Mokhtar, M. Z. M. Talib, E. H. Majlan, S. M. Tasirin, W. M. F. W. Ramli, W. R. W. Daud and J. Sahari, *J. Ind. Eng. Chem.*, 2015, **32**, 1–20.

116 G. A. Elia, K. Marquardt, K. Hoeppner, S. Fantini, R. Lin, E. Knipping, W. Peters, J. F. Drillet, S. Passerini and R. Hahn, *Adv. Mater.*, 2016, **28**, 7564–7579.

117 Y. Liu, Q. Sun, W. Li, K. R. Adair, J. Li and X. Sun, *Green Energy Environ.*, 2017, **2**, 246–277.

118 C. S. Li, Y. Sun, F. Gebert and S. L. Chou, *Adv. Energy Mater.*, 2017, **7**, 1–11.

119 A. Puapattanakul, S. Therdthianwong, A. Therdthianwong and N. Wongyao, *Energy Procedia*, 2013, **34**, 173–180.

120 M. Bockelmann, U. Kunz and T. Turek, *Electrochem. commun.*, 2016, **69**, 24–27.

121 J. Pan, L. Ji, Y. Sun, P. Wan, J. Cheng, Y. Yang and M. Fan, *Electrochem. commun.*, 2009, **11**, 2191–2194.

122 B. Pichler, B. S. Berner, N. Rauch, C. Zelger, H. J. Pauling, B. Gollas and V. Hacker, *J. Appl. Electrochem.*, 2018, **48**, 1043–1056.

123 Y. Li, M. Gong, Y. Liang, J. Feng, J. Kim, H. Wang, G. Hong, B. Zhang and H. Dai, *Nat. Commun.*, 2013, **4**, 1805.

124 J. Yi, P. Liang, X. Liu, K. Wu, Y. Liu, Y. Wang, Y. Xia and J. Zhang, *Energy Environ. Sci.*, 2018, **11**, 3075–3095.

125 K. Wang, P. Pei, Z. Ma, H. Chen, H. Xu, D. Chen and X. Wang, *J. Mater. Chem. A*, 2015, **3**, 22648–22655.

126 H. Kim, G. Jeong, Y. U. Kim, J. H. Kim, C. M. Park and H. J. Sohn, *Chem. Soc. Rev.*, 2013, **42**, 9011–9034.

127 C. Yang, J. Ming and C. Wu, *J. Power Sources*, 2009, **191**, 669–677.

128 L. Zhang, J. Cheng, Y. Yang and Y. Wen, *J. Power Sources*, 2008, **179**, 381–387.

129 M. Minakshi, D. Appadoo and D. E. Martin, *Electrochem. Solid-State Lett.*, 2010, **13**, A77–A80.

130 S. Ullah, A. Badshah, F. Ahmed, R. Raza, A. A. Altaf and R. Hussain, *Int. J. Electrochem. Sci.*, 2011, **6**, 3801–3811.

131 C. Zhang, J. M. Wang, L. Zhang, J. Q. Zhang and C. N. Cao, *J. Appl. Electrochem.*, 2001, **31**, 1049–1054.

132 R. Shivkumar, G. P. Kalaignan and T. Vasudevan, *J. Power Sources*, 1998, **75**,

View Article Online
DOI: 10.1039/C9TA10658H

90–100.

133 Y. Da Cho and G. T. K. Fey, *J. Power Sources*, 2008, **184**, 610–616.

134 C. Mele, A. Bilotta, P. Bocchetta and B. Bozzini, *J. Appl. Electrochem.*, 2017, **47**, 877–888.

135 J. F. Cooper, D. Fleming, L. Keene, A. Maimoni, K. Peterman, R. Koopman, Demonstration of Zinc/Air Fuel Battery to Enhance the Range and Mission of Fleet Electric Vehicles: Prelimi- nary Results in the Refueling of a Multicell Module, Lawrence Livermore National Laboratory, 1994.

136 P. Pei, S. Huang, D. Chen, Y. Li, Z. Wu, P. Ren, K. Wang and X. Jia, *Appl. Energy*, 2019, **241**, 124–129.

137 A. L. Zhu, D. P. Wilkinson, X. Zhang, Y. Xing, A. G. Rozhin and S. A. Kulinich, *J. Energy Storage*, 2016, **8**, 35–50.

138 S. Hosseini, S. J. Han, A. Arponwichanop, T. Yonezawa and S. Kheawhom, *Sci. Rep.*, 2018, **8**, 11273.

139 J. Lee, B. Hwang, M. S. Park and K. Kim, *Electrochim. Acta*, 2016, **199**, 164–171.

140 S. Hosseini, W. Lao-atiman, S. J. Han, A. Arpornwichanop, T. Yonezawa and S. Kheawhom, *Sci. Rep.*, 2018, **8**, 14909.

141 J. F. Parker, C. N. Chervin, I. R. Pala, M. Machler, M. F. Burz, J. W. Long and D. R. Rolison, *Science*, 2017, **418**, 415–418.

142 D. U. Lee, J. Y. Choi, K. Feng, H. W. Park and Z. Chen, *Adv. Energy Mater.*, 2014, **4**, 1301389.

143 P. Gu, M. Zheng, Q. Zhao, X. Xiao, H. Xue and H. Pang, *J. Mater. Chem. A*, 2017, **5**, 7651–7666.

144 B. Amunátegui, A. Ibáñez, M. Sierra and M. Pérez, *J. Appl. Electrochem.*, 2018, **48**, 627–637.

145 B. Pichler, S. Weinberger, L. Re, F. Gebetsroither, B. Bitschnau and V. Hacker, *Electrochim. Acta*, 2017, **251**, 488–497.

146 B. Pichler, S. Weinberger, L. Reščec and V. Hacker, *ECS Trans.*, 2017, **80**, 371–375.

147 D. U. Lee, H. W. Park, M. G. Park, V. Ismayilov and Z. Chen, *ACS Appl. Mater. Interfaces*, 2015, **7**, 902–910.

148 H. Bin Yang, J. Miao, S.-F. Hung, J. Chen, H. B. Tao, X. Wang, L. Zhang, R. Chen, J. Gao, H. M. Chen, L. Dai and B. Liu, *Sci. Adv.*, 2016, **2**, e1501122.

149 M. G. Park, D. U. Lee, M. H. Seo, Z. P. Cano and Z. Chen, *Small*, 2016, **12**, 2707–2714.

150 J. Zhang, L. Qu, G. Shi, J. Liu, J. Chen and L. Dai, *Angew. Chemie Int. Ed.*, 2016, **55**, 2230–2234.

151 L. T. Qu, Y. Liu, J. B. Baek and L. M. Dai, *ACS Nano*, 2010, **4**, 1321–1326.

152 K. Qu, Y. Zheng, S. Dai and S. Z. Qiao, *Nano Energy*, 2016, **19**, 373–381.

153 Y. Jiang, Y. P. Deng, J. Fu, D. U. Lee, R. Liang, Z. P. Cano, Y. Liu, Z. Bai, S. Hwang, L. Yang, D. Su, W. Chu and Z. Chen, *Adv. Energy Mater.*, 2018, **8**, 1702900.

154 J. Guo, T. Li, Q. Wang, N. Zhang, Y. Cheng and Z. Xiang, *Nanoscale*, 2019,

View Article Online
DOI: 10.1039/C9TA10658H

11, 211–218.

155 J. P. Zheng, P. Andrei, M. Hendrickson and E. J. Plichta, *J. Electrochem. Soc.*, 2011, **158**, A43–A46.

156 G. Girishkumar, B. McCloskey, A. C. Luntz, S. Swanson and W. Wilcke, *J. Phys. Chem. Lett.*, 2010, **1**, 2193–2203.

157 P. Vinatier, P. Stevens, G. Toussaint, C. Cantau and L. Puech, *J. Power Sources*, 2012, **214**, 330–336.

158 T. Wang, M. Yang and J. Pan, *Int. J. Electrochem. Sci.*, 2017, **12**, 6022–6030.

159 R. Black, B. Adams and L. F. Nazar, *Adv. Energy Mater.*, 2012, **2**, 801–815.

160 J. Huang and A. Faghri, *Electrochim. Acta*, 2015, **174**, 908–918.

161 X. Ren and Y. Wu, *J. Am. Chem. Soc.*, 2013, **135**, 2923–2926.

162 T. J. Simons, A. A. J. Torriero, P. C. Howlett, D. R. MacFarlane and M. Forsyth, *Electrochem. commun.*, 2012, **18**, 119–122.

163 A. R. Mainar, E. Iruin, L. C. Colmenares, A. Kvasha, I. de Meatza, M. Bengoechea, O. Leonet, I. Boyano, Z. Zhang and J. A. Blazquez, *J. Energy Storage*, 2018, **15**, 304–328.

164 F. Cheng and J. Chen, *Chem. Soc. Rev.*, 2012, **41**, 2172–2192.

165 A. Manthiram and L. Li, *Adv. Energy Mater.*, 2015, **5**, 1401302.

166 P. Tan, W. Kong, Z. Shao, M. Liu and M. Ni, *Prog. Energy Combust. Sci.*, 2017, **62**, 155–189.

167 D. Foster, K. Mutolo, J. Read, W. Behl, A. Driedger, M. Ervin and J. Wolfenstine, *J. Electrochem. Soc.*, 2003, **150**, A1351–A1356.

View Article Online
DOI: 10.1039/C9TA10658H

168 W. Lai and F. Ciucci, *Electrochim. Acta*, 2011, **56**, 4369–4377.

169 A. A. Franco and K.-H. Xue, *ECS J. Solid State Sci. Technol.*, 2013, **2**, M3084–M3100.

170 H. C. Lee, V. Roev, T. Y. Kim, M. S. Park, D. J. Lee, D. Im and S. G. Doo, *J. Power Sources*, 2016, **331**, 122–131.

171 L. Ye, W. Lv, K. H. L. Zhang, X. Wang, P. Yan, J. H. Dickerson and W. He, *Energy*, 2015, **83**, 669–673.

172 J. Zhang, J. Xiao, J.-G. Zhang, D. Wang and W. Xu, *J. Electrochem. Soc.*, 2009, **157**, A219–A224.

173 M. Safari, B. D. Adams and L. F. Nazar, *J. Phys. Chem. Lett.*, 2014, **5**, 3486–3491.

174 A. A. Shah, M. J. Watt-Smith and F. C. Walsh, *Electrochim. Acta*, 2008, **53**, 8087–8100.

175 M. Vynnycky, *Energy*, 2011, **36**, 2242–2256.

176 H. Al-Fetlawi, A. A. Shah and F. C. Walsh, *Electrochim. Acta*, 2010, **55**, 3192–3205.

177 H. Al-Fetlawi, A. A. Shah and F. C. Walsh, *Electrochim. Acta*, 2009, **55**, 78–89.

178 K. Oh, H. Yoo, J. Ko, S. Won and H. Ju, *Energy*, 2015, **81**, 3–14.

179 Y. Wang and S. C. Cho, *J. Electrochem. Soc.*, 2013, **160**, A1847–A1855.

180 S. S. Sandhu, J. P. Fellner and G. W. Brutchen, *J. Power Sources*, 2007, **164**, 365–371.

View Article Online
DOI: 10.1039/C9TA10658H

181 K.-H. Xue, T.-K. Nguyen and A. A. Franco, *J. Electrochem. Soc.*, 2014, **161**, E3028–E3035.

182 K. Tashiro, T. Masuda and F. Arai, *Electrochim. Acta*, 2015, **75**, 239–246.

183 K. Yoo, S. Banerjee and P. Dutta, *J. Power Sources*, 2014, **258**, 340–350.

184 U. Sahapatsombut, H. Cheng and K. Scott, *J. Power Sources*, 2013, **227**, 243–253.

185 U. Sahapatsombut, H. Cheng and K. Scott, *J. Power Sources*, 2013, **243**, 409–418.

186 X. Li, J. Huang and A. Faghri, *Energy*, 2015, **81**, 489–500.

187 F. Poli, L. K. Ghadikolaei and F. Soavi, *Appl. Energy*, 2019, **248**, 383–389.

188 S. Monaco, F. Soavi and M. Mastragostino, *J. Phys. Chem. Lett.*, 2013, **4**, 1379–1382.

189 F. De Giorgio, F. Soavi and M. Mastragostino, *Electrochem. commun.*, 2011, **13**, 1090–1093.

190 S. Monaco, A. M. Arangio, F. Soavi, M. Mastragostino, E. Paillard and S. Passerini, *Electrochim. Acta*, 2012, **83**, 94–104.

191 C. J. Allen, J. Hwang, R. Kautz, S. Mukerjee, E. J. Plichta, M. A. Hendrickson and K. M. Abraham, *J. Phys. Chem. C*, 2012, **116**, 20755–20764.

192 F. Soavi, S. Monaco and M. Mastragostino, *J. Power Sources*, 2013, **224**, 115–119.

193 F. Mizuno, K. Takechi, S. Higashi, T. Shiga, T. Shiotsuki, N. Takazawa, Y. Sakurabayashi, S. Okazaki, I. Nitta, T. Kodama, H. Nakamoto, H. Nishikoori,

View Article Online
DOI: 10.1039/C9TA10658H

S. Nakanishi, Y. Kotani and H. Iba, *J. Power Sources*, 2013, **228**, 47–56.

194 Z. H. Cui, W. G. Fan and X. X. Guo, *J. Power Sources*, 2013, **235**, 251–255.

195 L. Grande, E. Paillard, G. T. Kim, S. Monaco and S. Passerini, *Int. J. Mol. Sci.*, 2014, **15**, 8122–8137.

196 L. Grande, J. Von Zamory, S. L. Koch, J. Kalhoff, E. Paillard and S. Passerini, *ACS Appl. Mater. Interfaces*, 2015, **7**, 5950–5958.

197 J. Herranz, A. Garsuch and H. A. Gasteiger, *J. Phys. Chem. C*, 2012, **116**, 19084–19094.

198 L. Grande, A. Ochel, S. Monaco, M. Mastragostino, D. Tonti, P. Palomino, E. Paillard and S. Passerini, *Energy Technol.*, 2016, **4**, 85–89.

199 M. Olivares-Marín, P. Palomino, E. Enciso and D. Tonti, *J. Phys. Chem. C*, 2014, **118**, 20772–20783.

200 M. Piana, J. Wandt, S. Meini, I. Buchberger, N. Tsiouvaras and H. A. Gasteiger, *J. Electrochem. Soc.*, 2014, **161**, A1992–A2001.

201 E. Ventosa, D. Buchholz, S. Klink, C. Flox, L. G. Chagas, C. Vaalma, W. Schuhmann, S. Passerini and J. R. Morante, *Chem. Commun.*, 2015, **51**, 7298–7301.

202 J. Campos, Y. Gogotsi, E. C. Kumbur, K. W. Knehr, V. Presser and C. R. Dennison, *Adv. Energy Mater.*, 2012, **2**, 895–902.

203 T. Zhang and H. Zhou, *Nat. Commun.*, 2013, **4**, 1817.

204 F. Soavi, I. Ruggeri and C. Arbizzani, *ECS Trans.*, 2016, **72**, 1–9.

205 I. Ruggeri, C. Arbizzani and F. Soavi, *Carbon*, 2018, **130**, 749–757.

View Article Online
DOI: 10.1039/C9TA10658H

206 Q. Wang, S. M. Zakeeruddin, D. Wang, I. Exnar and M. Grätzel, *Angew. Chemie Int. Ed.*, 2006, **118**, 8377–8380.

207 F. Pan, J. Yang, Q. Huang, X. Wang, H. Huang and Q. Wang, *Adv. Energy Mater.*, 2014, **4**, 1400567.

208 Q. Huang, H. Li, M. Grätzel and Q. Wang, *Phys. Chem. Chem. Phys.*, 2013, **15**, 1793–1797.

209 Y. Chen, S. A. Freunberger, Z. Peng, O. Fontaine and P. G. Bruce, *Nat. Chem.*, 2013, **5**, 489.

210 D. Sun, Y. Shen, W. Zhang, L. Yu, Z. Yi, W. Yin, D. Wang, Y. Huang, J. Wang, D. Wang and J. B. Goodenough, *J. Am. Chem. Soc.*, 2014, **136**, 8941–8946.

211 Y. Wang, P. He and H. Zhou, *Adv. Energy Mater.*, 2012, **2**, 770–779.

212 Y. G. Zhu, C. Jia, J. Yang, F. Pan, Q. Huang and Q. Wang, *Chem. Commun.*, 2015, **51**, 9451–9454.

213 Y. G. Zhu, X. Wang, C. Jia, J. Yang and Q. Wang, *ACS Catal.*, 2016, **6**, 6191–6197.

214 Y. G. Zhu, F. W. T. Goh, R. Yan, S. Wu, S. Adams and Q. Wang, *Phys. Chem.*, 2018, **20**, 27930–27936.

215 M. Balaish, A. Kraytsberg and Y. Ein-Eli, *ChemElectroChem*, 2014, **1**, 90–94.

216 F. Xing, H. Zhang and X. Ma, *J. Power Sources*, 2011, **196**, 10753–10757.

217 A. Tang, J. McCann, J. Bao and M. Skyllas-Kazacos, *J. Power Sources*, 2013, **242**, 349–356.

View Article Online
DOI: 10.1039/C9TA10658H

218 F. T. Wandschneider, S. Röhm, P. Fischer, K. Pinkwart, J. Tübke and H. Nirschl, *J. Power Sources*, 2014, **261**, 64–74.

219 S. König, M. R. Suriyah and T. Leibfried, *J. Power Sources*, 2015, **281**, 272–284.

220 H. Fink and M. Remy, *J. Power Sources*, 2015, **284**, 547–553.

221 S. Huang, Z. Cui, N. Zhao, J. Sun and X. Guo, *Electrochim. Acta*, 2016, **191**, 473–478.

222 S. Meini, N. Tsiouvaras, K. U. Schwenke, M. Piana, H. Beyer, L. Lange and H. A. Gasteiger, *Phys. Chem. Chem. Phys.*, 2013, **15**, 11478–11493.